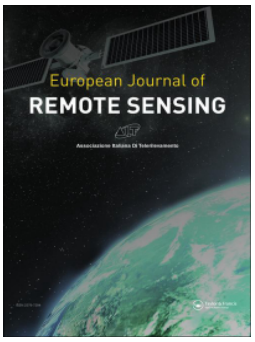

European Journal of Remote Sensing

ISSN: 2279-7254 (Online) Journal homepage: www.tandfonline.com/journals/tejr20

Estimating stand metrics in mountainous temperate forests using UAS and satellite imagery: multiple linear regression or artificial neural networks?

Hasan Aksoy , Alkan Günlü & Joel Kostensalo

To cite this article: Hasan Aksoy , Alkan Günlü & Joel Kostensalo (2026) Estimating stand metrics in mountainous temperate forests using UAS and satellite imagery: multiple linear regression or artificial neural networks?, European Journal of Remote Sensing, 59:1, 2697337, DOI: 10.1080/22797254.2026.2697337

To link to this article: https://doi.org/10.1080/22797254.2026.2697337

EUROPEAN JOURNAL OF REMOTE SENSING
2026, VOL. 59, NO. 1, 2697337
https://doi.org/10.1080/22797254.2026.2697337

Taylor & Francis by informa

RESEARCH ARTICLE

OPEN ACCESS Check for updates

Estimating stand metrics in mountainous temperate forests using UAS and satellite imagery: multiple linear regression or artificial neural networks?

Hasan Aksoy[a,b], Alkan Günlü[c] and Joel Kostensalo[b]

[a]Department of Forestry, Program of Forestry and Forest Products, Vocational School of Ayancık, Sinop University, Sinop, Türkiye; [b]Natural Resources Institute Finland, Joensuu, Finland; [c]Department of Forestry Engineering, Faculty of Forestry, Çankırı Karatekin University, Çankırı, Türkiye

ABSTRACT

Economically and environmentally sustainable utilization of forest resources requires monitoring, but extensive field surveys require, and the deployment of high-quality LiDAR sensors is not always economically viable. However, optical imagery collected either by satellite or an unmanned aircraft system (UAS) is available even in remote areas. We predicted stand volume (V), dominant height (h_{dom}), number of trees (N), basal area (BA) and quadratic mean diameter (dq), using images collected by Landsat 8 OLI (L8), Sentinel-1, Sentinel-2 (S2) and a UAS in natural pure Scots pine stands located in Northern Türkiye, which as a mountainous forested region presents a challenging test case. The stand metrics were modeled using multiple linear regression and artificial neural networks (ANNs) trained using Bayesian learning methods. Highest performance was found using L8 data for V ($R^2 = 0.84$, logRMSE = 0.34) and S2 data for N ($R^2 = 0.70$, logRMSE = 0.34), BA ($R^2 = 0.78$, logRMSE = 0.31), h_{dom} ($R^2 = 0.82$, logRMSE = 0.19) and dq ($R^2 = 0.83$, logRMSE = 0.07). The optimal orientation and window size varied depending on the stand characteristic. The ANN performed well for V ($R^2 = 0.83$, logRMSE = 0.38), N ($R^2 = 0.81$, RMSE = 0.34), BA ($R^2 = 0.84$, logRMSE = 0.27), h_{dom} ($R^2 = 0.71$, logRMSE = 0.25) and dq ($R^2 = 0.89$, logRMSE = 0.19). Stand metrics can be predicted in topographically challenging areas to a high accuracy using openly available satellite data.

ARTICLE HISTORY
Received 19 February 2026
Revised 7 May 2026
Accepted 26 June 2026

KEYWORDS
Satellite; UAS; artificial neural network; stand metrics; temperate forest; remote sensing

Introduction

Forests are functionally and structurally diverse terrestrial ecosystems, playing a significant role in human life (Chen et al., 2021). Besides providing wood-based products, forests also have ecological, environmental and socio-cultural roles in society (Gebreslasie et al., 2010). Monitoring stand metrics is crucial for the sustainable management of forests (Zahriban Heasari et al., 2019; Bulut et al., 2023a). Stand metrics have traditionally been derived from ground measurements, but conducting these measurements is particularly challenging in mountainous and dense forests, like those in Türkiye, due to the labor-intensive nature of such undertakings (Mohammadi et al., 2011).

Remote sensing (RS) data provide a cost-effective alternative to field data, enabling repeated observations and stand-level predictions (Lu, 2006). Optical images with high temporal and spatial resolution are particularly valuable for dynamic forest monitoring due to their availability, coverage, resolution and manageable computational demands (Aksoy, 2024a; Günlü et al., 2021). RS data, especially from satellites with broad spectral ranges, are widely used to predict stand metrics over large areas (Tuominen & Haakana, 2005). Advances in satellite imagery with enhanced spectral, spatial and radiometric properties enable more accurate estimation of stand metrics while reducing the need for extensive ground measurements and lowering costs (Delegido et al., 2011; Dube & Mutanga, 2015). The use of Unmanned Aircraft Systems (UASs) has also recently become popular in forestry applications (Kalbi, 2011; Kameyama &

CONTACT Joel Kostensalo joel.kostensalo@luke.fi Natural Resources Institute Finland, Yliopistokatu 6B, FI-80100 Joensuu, Finland
Supplemental data for this article can be accessed online at https://doi.org/10.1080/22797254.2026.2697337.

Sugiura, 2020; Krause et al., 2019). The ability to optimize flight and imaging parameters such as camera angle, flight altitude, acquisition time, spatial resolution and image overlap grants UASs a level of flexibility and precision that surpasses satellite-based data sources. Their very high spatial resolution (2.5–3.5 cm), capability for repeated data acquisition and customizable flight plans tailored to site-specific conditions provide substantial advantages for the accurate estimation of forest stand parameters (White et al., 2016). In recent years, in the monitoring of natural resources, the joint or comparative analysis of multi-source datasets with different spatial, spectral and temporal characteristics has become increasingly important, rather than approaches relying on a single remote sensing platform. Optical satellite remote sensing is widely used in environmental monitoring studies due to its capacity for wide-area and long-term observation (Kutser et al., 2009; Qiu et al., 2025; Shi et al., 2019). However, factors such as cloud cover, precipitation, imaging time and relatively coarse spatial resolution can prevent satellite data from adequately representing the high heterogeneity at the local scale or meeting urgent monitoring requirements with sufficient detail (Qiu et al., 2025). Due to these limitations, the joint analysis of satellite, UAS and ground based observations as complementary data sources with distinct spatial and temporal advantages is becoming increasingly important for monitoring environmental variability in a more detailed and comprehensive manner (Kwon et al., 2020; Qiu et al., 2025).

The Landsat program has been a widely used source of freely available satellite images since 1972 (Phiri & Morgenroth, 2017). More recently, the Sentinel-2 satellite series (EU Copernicus program) has offered improved data for forest monitoring, featuring four additional spectral bands sensitive to chlorophyll changes, higher accuracy and better cost efficiency compared to Landsat (David et al., 2022). Sentinel-2 also has a higher spatial resolution, enabling more detailed vegetation information (Jiang et al., 2022). Besides optical sensors, active satellite technologies like LiDAR and Synthetic Aperture Radar (SAR) are also employed for estimating stand metrics (Keleş et al., 2021; Sinha et al., 2015). Models based solely on short-wavelength SAR images generally perform worse than those using P, L bands alongside passive satellite data (Güverçin & Günlü, 2023).

Forest stand characteristics have been predicted in the literature using Multiple Linear Regression (MLR), as well as machine-learning approaches such as *k* Nearest Neighbor (*k*NN), Support Vector Machine (SVM), Random Forest (RF) (Aksoy, 2024b), Bayesian Additive Regression Trees (BART), Classification and Regression Tree (CART) and Artificial Neural Network (ANN) techniques (Ozkan & Demirel, 2018; Wu et al., 2016; Turgut and Günlü, 2022; Bulut, 2023b). However, assumptions of linearity and distribution are known to affect the performance of parametric models (Were et al., 2015; Zhao et al., 2019). While these problems can be tackled by transforming variables or using generalized additive models, it may be laborious to find the optimal model. On the other hand, machine-learning methods often do not need to make any assumptions at all (Andersen, 2009; Thanh Noi & Kappas, 2017) and have thus been commonly employed during the past decade (Ahmadi et al., 2020; Keleş et al., 2021; Zhao et al., 2019).

ANN and MLR are commonly used to estimate forest stand metrics from remote sensing data because they effectively capture relationships between spectral, textural and structural variables and stand variables. MLR is often favored for its statistical transparency and ease of interpretation (Hudak et al., 2002; Mutlu et al., 2008). Conversely, ANNs have shown superior performance in modeling complex and nonlinear interactions, offering greater flexibility in handling high-dimensional and multicollinear datasets (Ozkan et al., 2012; Zhang et al., 2019). ANNs are especially useful when data variability arises from factors like forest type, topography, or sensor differences. Moreover, comparative studies show that both ANN and MLR often achieve competitive or better prediction accuracy than other machine-learning methods like RF, particularly when training the data are limited (Fassnacht et al., 2016; Latifi et al., 2015). The widespread use of both ANN and MLR reflects a balance between model performance, interpretability and practicality. Although ANNs are capable of modelling complex and non-linear relationships between remote-sensing predictors and forest stand parameters, they may be prone to overfitting, particularly when the number of predictors is high relative to the number of training samples. Therefore, appropriate training and regularization strategies, such as Bayesian regularization and early stopping procedures, are commonly used to improve model generalization and reduce overfitting risk (Bolat, 2021; Okut, 2016; Skudnik & Jevšenak, 2022).

Machine learning methods have proven effective for predicting stand metrics in temperate forests (Ahmed et al., 2015; Sakıcı and Günlü, 2018; Ahmadi et al., 2020; Bulut et al., 2024; Günlü et al., 2021). Despite many studies predicting stand metrics, comprehensive comparisons between satellite and UAS optical imagery are rare in the literature, and completely lacking for natural Scots pine forests. The mountainous terrain of Northern Türkiye and the complexity of natural stands, provide a truly challenging environment requiring significant robustness from the models. In this work, we compare the predictive performance of datasets derived from satellite imagery (L8, S1 and S2) and cost effective RGB sensor based UAS imagery in natural pure Scots pine forests located in mountainous regions. Our study differentiates itself by processing and comparing UAS and satellite imagery through methodologically consistent workflows, where feature extraction and modeling follow the same steps for both UAS and satellite data. A distinctive aspect of this study is the systematic optimization of ANN hyperparameters (learning rate and momentum). This study provides a detailed evaluation of how MLR and ANN perform across different RS data sources, while also identifying the most influential variables for predicting key stand characteristics, thereby offering practical insights for forest managers, planners and researchers seeking efficient and scalable inventory solutions.

Material and methods

Study area

This study was carried out in the Sinop Regional Directorate of Forestry (RDF) located in the northern part of Türkiye between the longitudes of 34° 10′ 26″ and 35° 30′ 06″ E and the latitudes of 42° 05′ 30″ and 41° 20′ 30″ N in Pure Scots pine (*Pinus sylvestris* L.) stands (Figure 1). The study area receives the highest rainfall in October and the lowest in May, with an average annual precipitation of 685.7 mm. The annual average temperature is 14 °C (GDF, 2022).

Data

Ground measurements of volume (V), basal area (BA), quadratic mean diameter (dq), dominant height (h_{dom}) and stem density (N) were collected from 184 sample plots covering various development stages,

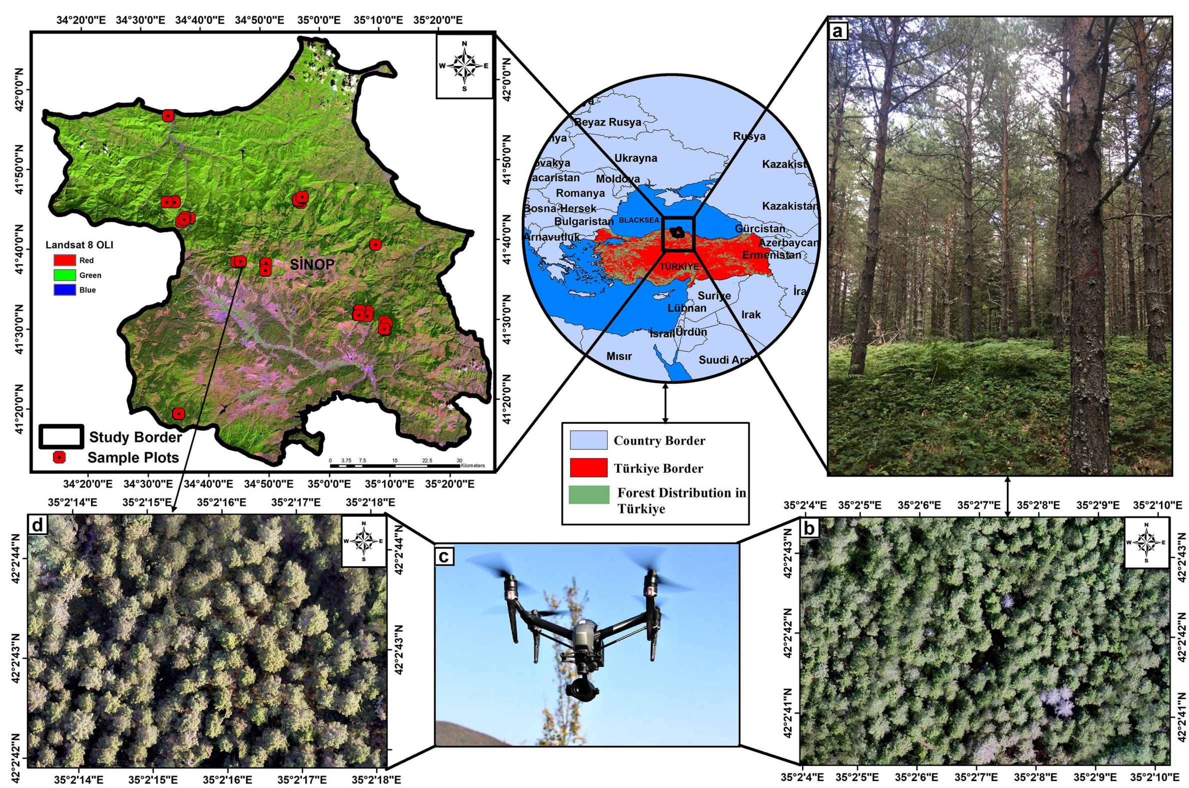

Figure 1. Map of the study area. (a) An example image of the sample plot where ground measurements were conducted; (b, d) example digital UAS orthomosaic images of the study area; (c) UAS used in the study.

canopy closures and site qualities. RSdata included S1, S2, L8 satellite images and UAS images. The S1 dual-polarized VV/VH image from October 17, 2021, was obtained from ESA's Copernicus Access Hub. S2 images dated October 15, 2021, with 13 spectral bands at resolutions of 10 m, 20 m and 60 m and L8 images from September 26, 2021, with 11 spectral bands at resolutions of 15 m, 30 m and 100 m, were acquired from the USGS Earth Explorer. UAS images were captured between August and October 2021 using a DJI Inspire-2 drone equipped with a Zenmuse X-5S sensor. Because the UAS lacked Real-Time Kinematic (RTK) capability, centimeter-precision Ground Control Points (GCPs) were established with GNSS receivers to improve positional and altitude accuracy (Figure 2).

Ground measurements

Traditional forest inventory measurements were conducted on 184 circular plots. Sample plot sizes were chosen depending on forest canopy closure: 400 m^2 for fully covered stands (71%–100%), 600 m^2 for medium closure stands (41%–70%) and 800 m^2 for scattered stands (11%–40%). The diameter at breast height (DBH) of all trees with DBH ≥ 8 cm was recorded. In young stands, trees with a DBH of less than 8 cm were also included. Additionally, the number of trees was determined in each sample plot, and the heights of a sufficient number of dominant and co-dominant trees were measured to determine the dominant height of the stand according to the 100-tree method per hectare, and the stand metrics were calculated based on these (Table 1). The single-entry Scots pine volume equation (see Equation (1)) developed for the Western Black Sea Region ($R^2 = 0.993$), was used (Yavuz et al., 2010) for volume estimation:

$$\ln(V) = -8.209 + 2.324d - \frac{3.664}{d}, \tag{1}$$

where V is the volume, d is the DBH (diameter at 1.3 m) and ln is the natural logarithm.

Satellite and UAS data

RS data from S1, S2, L8 and UAS images were utilized. S1 images were preprocessed using SNAP software, calculating backscatter (dB) and band reflectance for VV and VH polarizations. The preprocessing in SNAP via 'Graph Builder' included eight steps: reading the image, applying orbit files, thermal noise removal, calibration, speckle filtering, terrain correction, conversion from dB to linear scale and saving the image. The preprocessed S1 raster layers were then imported into ArcGIS 10.7 and spatially overlaid with the circular sample plot polygons. The plot polygons were used as zonal units to extract plot level VV and

DJI Inspire 2	
Maximum take-off weight	8.82lbs (4000g)
Maximum flight time	Approx. 27 min (with zenzenx4s)
Operating temperature	-4° to 104°F (-20° to 40°C)
Battery capacity	4280mAh
Maximum speed	58 mph or 94 kph (sport mode)
Energy	97.58Wh
Voltage	22.8V
Type	quadcopter
Live view	1080p
DJI Zenmuse X-5S	
5.2K video recording at 30fps and 4K at 60fps	
20.8 MP still image capture	
12.8 stops of dynamic range	
12-bit raw photos	
20fps continuous burst shooting	

Figure 2. Technical specifications of the DJI Inspire 2 UAS platform and DJI Zenmuse X5S optical sensor used for UAV image acquisition.

Table 1. Formulae for the calculation of stand metrics.

Stand parameter	Formula	Variables
d_g [cm]	$\bar{d}_g = \frac{1}{n} \sqrt{\sum_{i=1}^{n} \bar{d}_i^2}$	d_g = quadratic mean diameter $d_1,\ldots,d_n$ = measured tree diameter n = no. of measured trees
h_{dom} [m]	$h_{dom} = \frac{1}{n} \sum_{i=1}^{n} h_i$	h_{dom} = dominant height $h_1 \ldots h_n$ = measured tree heights (100 tallest per hectare)
N [trees/ha]	$N = \frac{10000}{SPS} \times n$	N = no. of stand trees (ha) SPS = sample plot size (m^2)
BA [m^2/ha]	$BA = \frac{10000}{SPS} \times g$	BA = stand basal area (ha) g = basal area of the sample plot
V [m^3/ha]	$V = \frac{10000}{SPS} \times \sum_{i=1}^{n} v_i$	V = stand volume (ha) v_i = volume of tree i

VH values from the S1 raster layers using ArcGIS's 'zonal statistics' tool. Thus, dB and digital band values for VV and VH polarizations were calculated for each plot (Aksoy, 2022).

S2 and L8 images were preprocessed in QGIS 3.8.1 using the Semi-Automatic Classification Plugin (SCP) only for radiometric preprocessing and the derivation of band reflectance values. No thematic or land cover classification was performed in this step. The resulting reflectance raster layers were imported into ArcGIS 10.7 and spatially overlaid with the circular sample plot polygons based on canopy closure. Plot level reflectance values were extracted from each raster layer using ArcGIS's 'zonal statistics' tool, and VIs were computed from these values (Supplementary material, Table S1). Additionally, texture datasets were generated in ENVI 5.2 using S2 and L8 images, including eight texture features—mean (M), correlation (COR), variance (VAR), homogeneity (HOM), dissimilarity (DIS), contrast (CONT), second moment (SM) and entropy (ENT)—calculated for four orientations (0°, 45°, 90°, 135°) and seven window sizes (3 × 3 to 15 × 15). In total, 3808 texture datasets were produced using 17 bands, 8 features, 7 window sizes and 4 orientations. Each pixel is analyzed with its surrounding neighborhood based on the window size, representing spatial resolution. Small windows capture leaf details, while larger ones detect tree group boundaries more accurately. Image orientation reflects the angle of structural features in satellite data (Haralick et al., 1973). The inclusion of texture metrics in the modeling process of this study aimed to accurately represent the structural characteristics and spatial heterogeneity of forest cover. This is because GLCM (Gray-Level Co-occurrence Matrix)-based metrics such as contrast, homogeneity, entropy and variance capture the reflectance properties of surface elements, including tree crowns, shadows, gaps and understory vegetation, within a spatial context, thereby complementing the limited discriminative power of spectral data (Haralick et al., 1973). Smaller window sizes (3 × 3–5 × 5) capture the local variability of individual trees or small clusters, whereas larger windows (11 × 11–15 × 15) represent the overall stand-level structure and heterogeneity (Pu & Landry, 2012). By utilizing varying window sizes, the spatial structure at both individual tree and stand scales can be modeled separately.

UAS images were acquired using a DJI Inspire 2 UAS platform equipped with a DJI Zenmuse X5S optical camera. The Zenmuse X5S camera includes a 4/3″ CMOS sensor with a resolution of 20.8 MP and a pixel size of 3.4 µm. A 15 mm focal length lens was used during image acquisition. The technical specifications of the UAS platform and optical sensor are presented in Figure 2. Ground control points were established beforehand, and flight plans were prepared based on the UAS's battery limits. Takeoff points and altitude data were extracted for each plan, and the minimum altitude was determined. A uniform flight altitude of 120 m was set for all plots. Side and front overlap ratios were set at 70% and 80%, respectively, and the camera angle was fixed at 90° (Nadir). Flights were conducted between 11am and 3pm under minimal cloud cover to ensure optimal lighting and image quality. Orthomosaics, digital terrain models (DTM), digital surface models (DSM) and reflectance images were produced. All images contained three bands (red, green, blue) and an additional grayscale (panchromatic) band (Equation (2)), generated to support vegetation index calculations (Aksoy & Günlü, 2025).

$$\text{Grey scale} = 0.2126 \times \text{Red} + 0.7152 \times \text{Green} + 0.0722 \times \text{Blue}. \tag{2}$$

UAS image processing was carried out in three stages using Pix4D software (Figure 3). First, images were aligned and calibrated with camera parameters and ground control points for precise geographic positioning. Next, point clouds and solid models were generated, classified and used to create a digital terrain model (DTM) and 3D textured models. Finally, a DSM filter was applied to produce DSM,

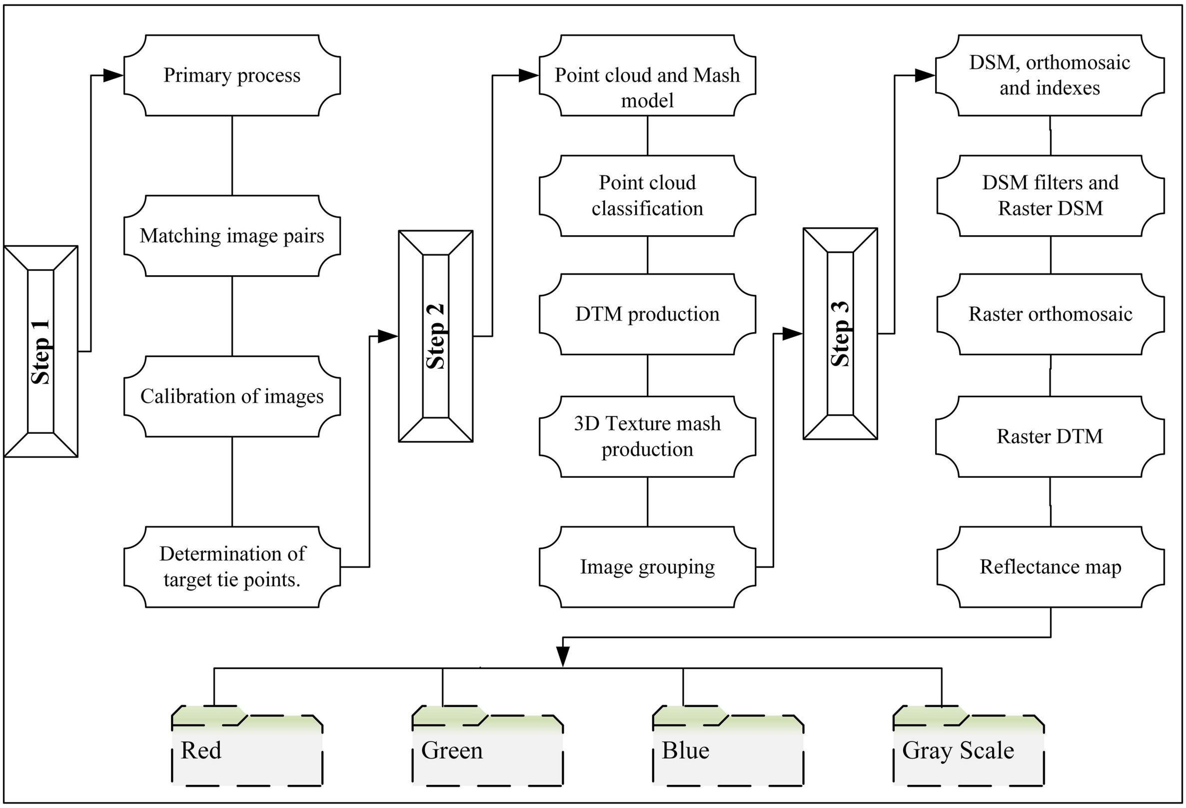

Figure 3. The general UAS image processing methodology.

orthomosaic and DTM raster images, which were combined into reflectance images for the study area. An example is shown in Figure 4.

Sixteen UAS flights were conducted to cover the plots. Fifteen vegetation indices were calculated from UAS data, adding to those from satellite images, resulting in 39 vegetation indices for modeling (Table S1). The dataset was created by converting S2, L8 and UAS image bands into vector layers in ArcGIS, overlaying them with plot polygons. For the modelling analyses, the remote sensing derived variables obtained from UAS, S1, S2 and L8 data were organized into 31 input datasets according to sensor type, data type, vegetation indices, reflectance values, backscattering values and GLCM-based texture configurations. These datasets were generated to evaluate the predictive contribution of different remote sensing data groups rather than individual variables. The descriptions of the remote-sensing-derived datasets used as input datasets in the modelling process are presented in Table S1a.

Models

The modeling workflow is shown in Figure 5. In this study, the modeling process was structured in two stages. In the first stage, 31 different remote sensing datasets were modeled separately using the MLR technique for the parameters V, BA, N, h_{dom} and dq. These datasets consist of UAS based digital number values, UAS and satellite-based vegetation indices, reflectance values, S1 backscatter values and GLCM-based texture datasets derived from different window sizes and orientations. Tables S2–S4 (in the Supplementary material) represent the different input datasets, with each row corresponding to a separate modeling scenario. All candidate variables within each dataset were included in the stepwise MLR algorithm, and only those found to be statistically significant were retained in the final model (Table S5).

In the second stage, the dataset yielding the best results in the MLR analysis was identified for each stand parameter, and the significant variables selected from this dataset (Table S5) were used as input variables in the ANN modeling. Thus, the ANN models were developed not using the entire high-

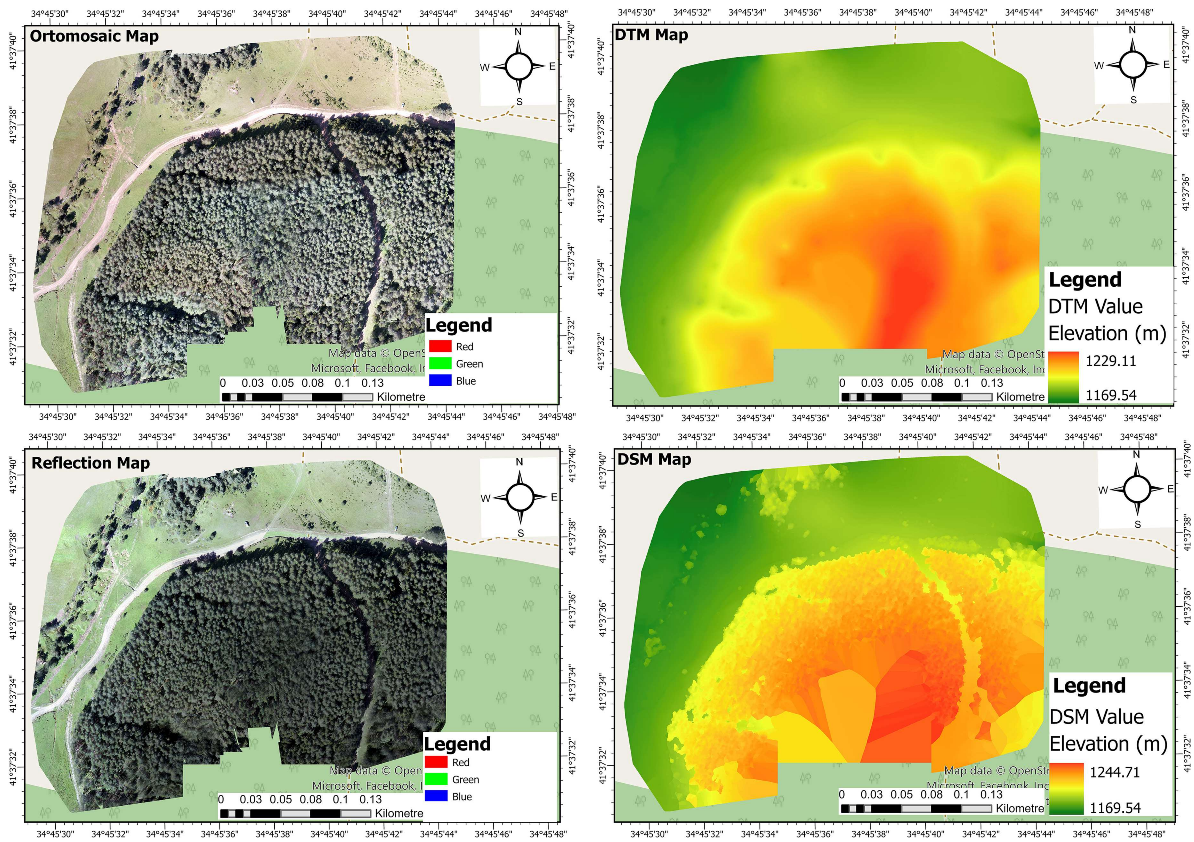

Figure 4. Image series created with UAS imagery (Example parcel, Sakız Planning Unit).

dimensional dataset, but rather using groups of variables that had been filtered by MLR and proven to be statistically significant. The dataset was randomly divided into two subsets: 80% (150 plots) for model development and 20% (34 plots) for testing. After estimating forest cover using MLR and ANN, the Bland–Altman method was used to assess whether there were any significant differences between the two modeling techniques. The UAS models DN and VIs were modelled without transforming the response variable, and the satellite models and UAS RV with log-transformed response variables.

Multiple linear regression analysis

A stepwise MLR algorithm was utilized to predict stand metrics with the level of statistical significance set at $p = 0.05$. IBM SPSS 21 software was used. MLR analyses were performed separately for each stand parameter using 31 different remote sensing derived input datasets. Each input dataset represents a specific combination of sensor, feature group, texture orientation, or window size. Depending on the input dataset, the candidate predictor variables in the MLR analyses included DN values, RV values, VIs, S1 back-scattering values and GLCM-based texture metrics derived from UAS, S1, S2 and L8 data. VIs were included in the UAS VIs, S2 VIs and L8 VIs datasets, whereas the remaining datasets consisted of sensor-specific spectral, backscattering, or texture-derived variables. The 31 remote-sensing-derived input datasets are described in Table S1a. All candidate variables in the relevant dataset were included in the stepwise MLR process, and variables found to be significant at the $p \leq 0.05$ level were retained in the final model. In the stepwise MLR procedure, the contribution of each candidate variable was evaluated after accounting for the predictors already included in the model. Therefore, variables that did not provide additional independent explanatory information, including variables carrying redundant or highly overlapping information with the retained predictors, were excluded from the final model. In this way, the stepwise selection process was used to obtain a parsimonious predictor set and to reduce collinearity-related redundancy within each dataset-specific MLR model. This approach was used to compare the predictive

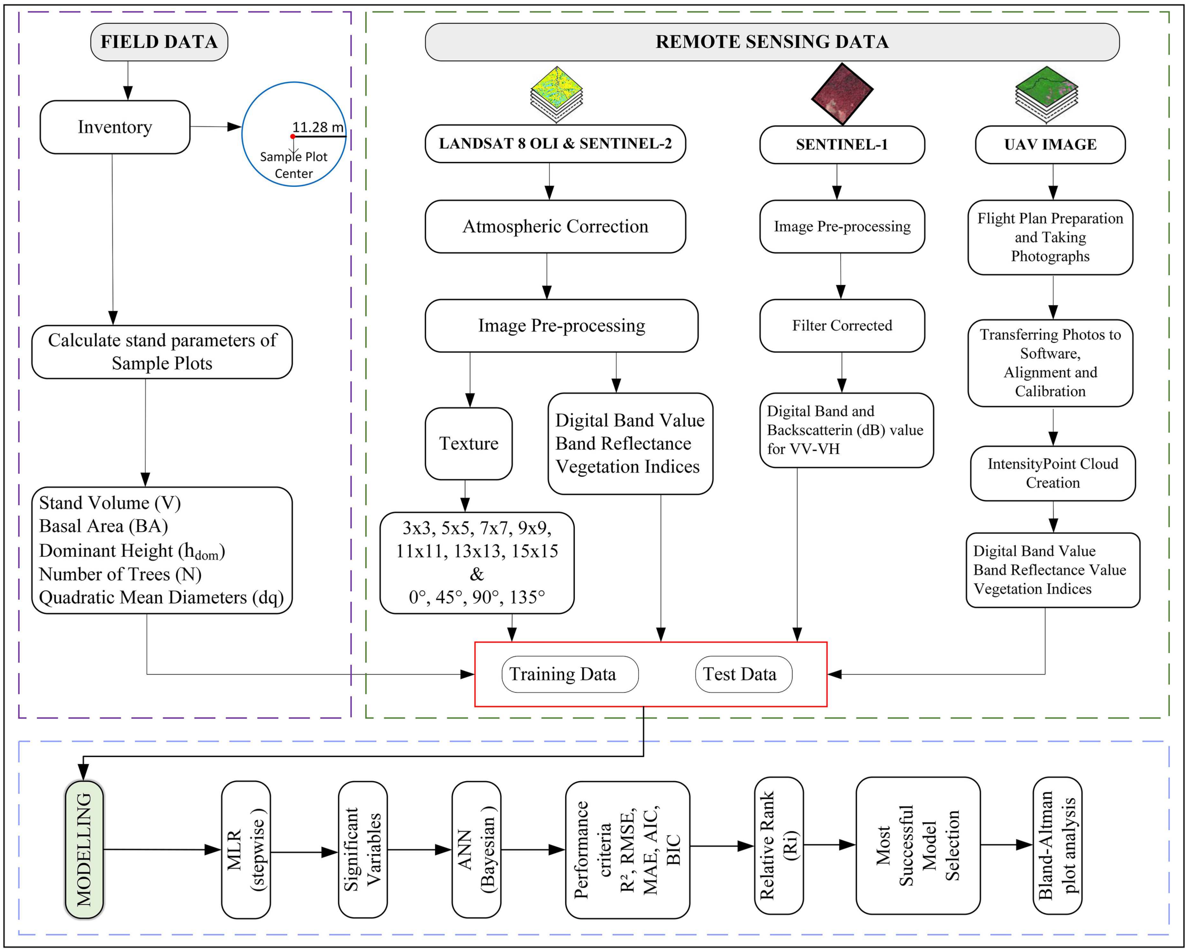

Figure 5. Flowchart of the methodology utilized in this study.

performance of different remote-sensing-derived datasets and to reduce predictor redundancy, collinearity-related effects and overfitting risk arising from the large number of spectral, index based and texture derived variables. Using the performance metric values presented in Tables S2–S4, the performance metrics of the MLR models created for each parameter using the relevant dataset were evaluated. The response variable M_i (dq, h_{dom}, N, BA, or V) for the plot i is given by the equation

$$M_i = \beta_0 + \sum_{j=1}^{n} \beta_j X_{j,i} + \varepsilon_i, \tag{3}$$

where $X_{1,i}$, $X_{2,i}$, …, $X_{n,i}$ denote the features for the plot I, which have been obtained from L8, S2, S1 and UAS images, β_0, β_1, β_2……β_n are the regression coefficients, and ε_i is a normally distributed error term.

Artificial neural networks

ANN models were implemented in MATLAB using a feed-forward neural network architecture (Bolat, 2021). The input variables used in the ANN models were determined through an MLR-based pre-selection process. In the first stage, 31 different remote-sensing-derived input datasets were tested separately using MLR for each stand parameter, and the best-performing dataset was identified. Subsequently, the statistically significant variables retained in the best performing MLR model were selected and used as input variables in the ANN model for the corresponding stand parameter (Table S5). Thus, ANN modelling was performed using MLR selected predictors with statistically supported explanatory power rather than the entire high dimensional RS dataset. This two stage modelling strategy was applied to reduce the influence of unnecessary or weak explanatory variables, control model complexity and reduce overfitting risk under limited sample size conditions. For each stand parameter, the ANN input layer consisted of the significant predictors selected from the corresponding best performing MLR model. Therefore, the number of input neurons varied according to the parameter-specific variable set presented in Table S5. The network architecture consisted of one hidden layer with two neurons and one output neuron representing the target stand parameters. A hyperbolic tangent sigmoid transfer function was used as the activation function in the hidden layer, while the output layer was used to produce continuous standard parameter estimates. Before training, input and output variables were normalized to the range of −1 to +1 using the *mapminmax* function to improve numerical stability and model generalization (Foresee & Hagan, 1997). Bayesian regularization backpropagation was used as the training algorithm. In this procedure, the objective function considers both prediction error and the magnitude of network weights, thereby penalizing overly complex weight structures and improving the generalization ability of the network. Therefore, Bayesian regularization was used as the main regularization mechanism to reduce overfitting risk, particularly because the number of observations was limited relative to the number of remote-sensing-derived predictors (Foresee & Hagan, 1997).

To evaluate the effect of training parameters on ANN performance, 17 different ANN configurations were tested for each stand parameter. In the remaining eight configurations, the learning rate was varied from 0.2 to 0.9 while the momentum coefficient was fixed at 0.1. In the remaining eight configurations, the learning rate was varied while the momentum coefficient was fixed at 0.1. Learning rate and momentum parameters were evaluated because they may influence convergence behavior, training stability and prediction error in ANN modelling (Lawrence et al., 1997). Each ANN configuration was trained and evaluated separately, and the configuration providing the best predictive performance was selected as the final ANN model for the corresponding stand parameter. Repeated training runs were also performed to reduce the influence of random initialization of network weights and biases.

Model performance criteria

The predictive model performance was evaluated based on the coefficient of determination (R^2_{adj}, Equation (4)), root mean squared error (RMSE, Equation (5)), mean absolute error (MAE, Equation (6)), bias (Equation (7)), as well as the Bayesian information criterion (BIC) and Akaike's information criterion (AIC). The relevant formulae are:

$$R^2_{\text{adj}} = 1 - \frac{(n-1)\sum_{i=1}^{n}(y_i - \hat{y}_i)^2}{(n-p)\sum_{i=1}^{n}(y_i - \overline{y}_i)^2}, \tag{4}$$

$$\text{RMSE} = \sqrt{\frac{1}{n}\sum_{i=1}^{n}(y_i - \hat{y}_i)^2}; \quad \log\text{RMSE} = \log(\text{RMSE}), \tag{5}$$

$$\text{MAE} = \frac{1}{n}\sum_{i=1}^{n}|y_i - \hat{y}_i|, \tag{6}$$

$$\text{Bias} = \frac{\sum_{i=1}^{n}(y_i - \hat{y}_i)}{n}. \tag{7}$$

High model performance is indicated by large R^2 values and small RMSE, MAE, Bias, BIC and AIC values. The Relative Ranking Method by Poudel and Cao (2013) was used to select the best model by considering all criteria (R_i), given by Equation (8):

$$R_i = 1 + \frac{(\text{m}-1)(S_i - S_{\min})}{S_{\max} - S_{\min}}. \tag{8}$$

This method ranks closeness and distance values for each criterion, sums the R_i scores and identifies the model with the lowest total R_i as the best performer (Ercanlı et al., 2018).

Results

The mean values for dq, h_{dom}, N, BA and V were 24.13 cm, 16.89 m, 884 stems ha^{-1}, 28.15 m^2 ha^{-1} and 259 m^3 ha^{-1} (Table 2). The volume range was 21–865 m^3 ha^{-1} and dominant height range 4.52–34.90 m.

Table 2. Descriptive statistics values for stand metrics.

Metrics	Min.	Max.	Mean	SD
dq (cm)	5.62	55.98	24.13	13.18
h_{dom} (m)	4.52	34.90	16.89	7.80
N (number ha^{-1})	100	2800	884	689
BA (m^2 ha^{-1})	4.20	79.41	28.15	19.40
V (m^3 ha^{-1})	21	865	259	225

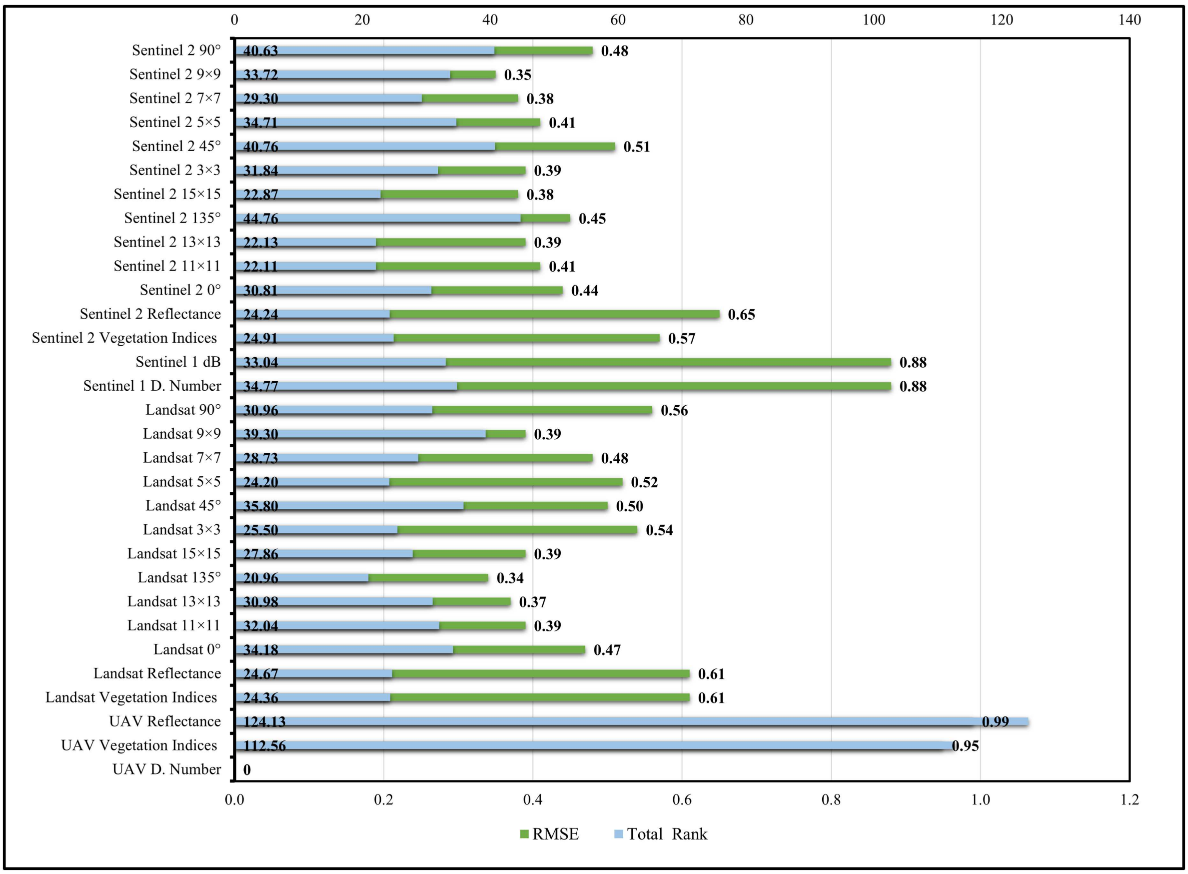

Figure 6. Variation in RMSE and total relative rank numbers of models derived from remote sensing data for MLR method (This graph for V, for the others see Supplementary material).

Multiple linear regression analysis

The MLR result tables are given in Supplementary material (Tables S2–S4) and Figures 6 and 7. Reflectance data from S2 resulted in best the best performance for V (logRMSE = 0.65), while UAS performance was low (RMSE = 190 m^3 ha^{-1}), though the numbers are not directly comparable. For vegetation indices, L8 performed best (logRMSE = 0.61), and UAS again relatively poor (RMSE = 179.07 m^3 ha^{-1}). Texture-based models performed best with S2 and a 11 × 11 window size (logRMSE = 0.41) and the worst for 3 × 3 window with L8 (logRMSE = 0.54). The best orientation for texture features was 135° in L8 (logRMSE = 0.34), and the worst was 190° in L8 (logRMSE = 0.56). UAS digital band values and S1 backscatter and digital number data did not result in reasonable models.

For BA, the best performance for reflectance was with L8 (logRMSE = 0.49), while UAS performance was poor (RMSE = 15.98 m^2 ha^{-1}). The best performance for vegetation indices was with S2 (logRMSE = 0.52) and again poor for UAS (RMSE = 14.87 m^2 ha^{-1}). For models based on texture features obtained from L8 and S2, the best performance was found for the 9 × 9 window size and S2 (RMSE = 0.31 m^2 ha^{-1}) and the worst with 5 × 5 window size and S2 (logRMSE = 0.35). The best orientation for texture features was found 0° (S2;

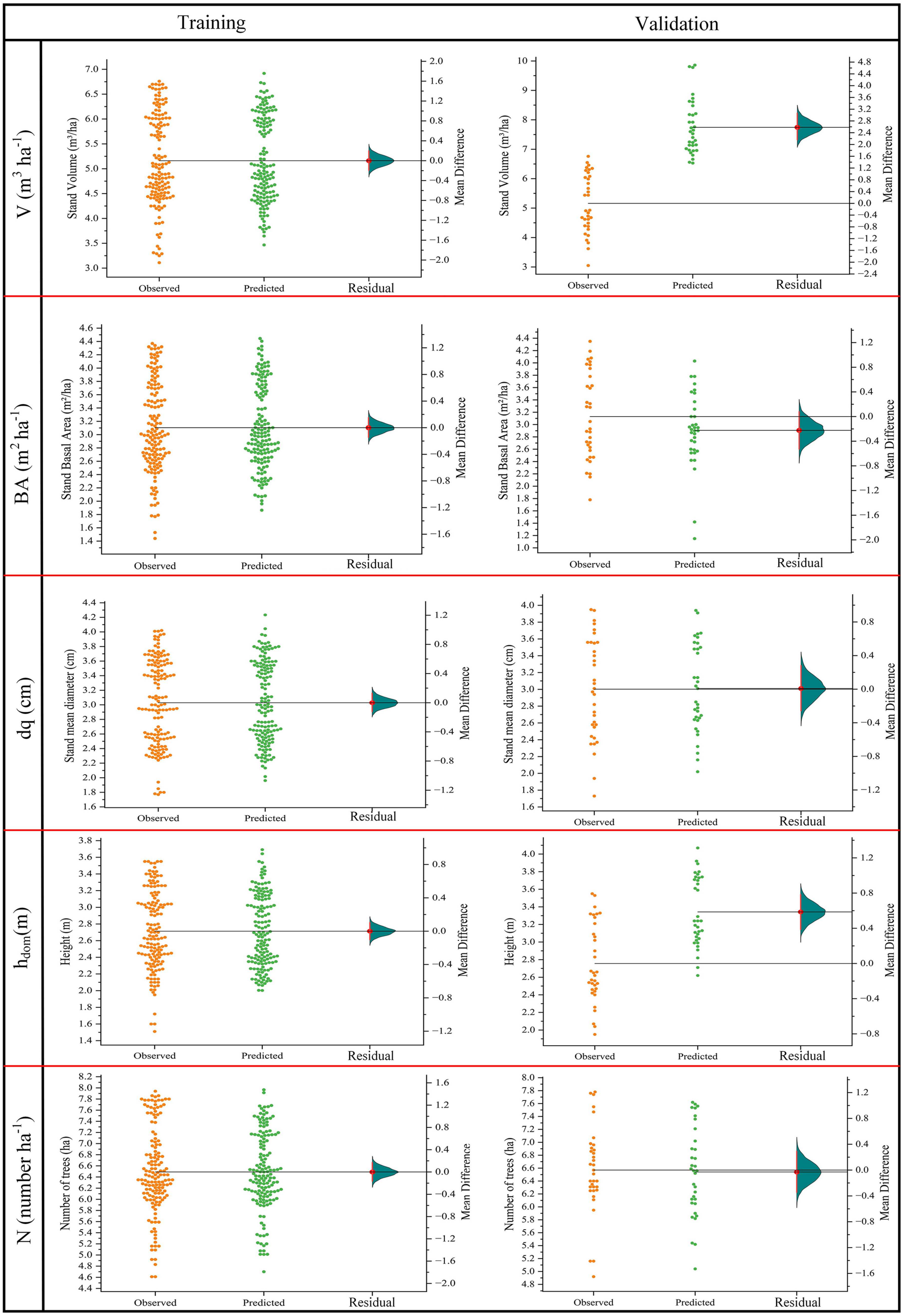

Figure 7. Observation, prediction and error distribution plot for multiple linear regression (for model and test) for the log-transformed metrics V, BA, N, h_{dom} and dq.

logRMSE = 0.30) and the worst was 45° (S2; logRMSE = 0.36). UAS digital band values could not predict BA. The performance of models using backscattering and digital number data of the S1 active satellite image was poor.

For *N* (Table S3), L8 performed best ($R^2 = 0.62$; logRMSE = 0.48) and UAS worst (logRMSE = 0.74). Vegetation indices worked best with S2 (logRMSE = 0.49) and poorly with UAS (RMSE = 639.80 number ha^{-1}). 15 × 15 window of S2 was optimal for texture-based models (logRMSE = 0.34) and 7 × 7 window of L8 was the worst (logRMSE = 0.36). For texture orientation, the best was 135° (S2; logRMSE = 0.41) and the worst was 90° (S2; logRMSE = 0.39). UAS digital bands or S1 backscatter/digital band data could not predict N.

For h_{dom}, reflectance performance was best with S2 (logRMSE = 0.25), and worst with L8 (logRMSE = 0.84). Vegetation indices performed best with S2 (logRMSE = 0.25) and badly with UAS (RMSE = 5.69 m). Among texture-based models, the 5 × 5 window of S2 had best performance (logRMSE = 0.19), and 3 × 3 window of S2 had the lowest (logRMSE = 0.22). For texture orientation, 90° of S2 performed best (logRMSE = 0.24), while 135° of L8 had the worst, though just measured on RMSE seems to perform well (logRMSE = 0.20). Models based on UAS digital band and reflectance data and S1 backscattering and digital bands performed poorly.

Finally, for dq, the best reflectance performance was found with L8 (logRMSE = 0.30), and the worst with S2 (logRMSE = 0.31). Vegetation indices performed best with L8 (logRMSE = 0.30). Among texture-based models, the 5 × 5 window of S2 was best (logRMSE = 0.21), while the 7 × 7 window of S2 was worst (logRMSE = 0.07). For texture orientation, 0° of S2 was best (logRMSE = 0.26) and 135° of L8 the worst (logRMSE = 0.23). UAS reflectance models and models utilizing S1 backscattering and digital band data performed poorly.

Artificial neural networks

Prediction of the stand metrics with ANNs was carried out using the RS data which performed best in the MLR modelling (Supplementary material Table S5). A total of 17 models were developed for each stand metric by applying different learning rates and momenta in the models (Figure 8, Tables S6–S8). For V, the highest R^2 and the lowest total relative rank were recorded in model V2 (Model $R^2 = 0.83$; logRMSE = 0.38, Test $R^2 = 0.77$; logRMSE = 0.47) (Table S6). Overall, although the $R^2$of models V4, V6 and V7 were higher and their total relative ranks were lower compared to model V2, they were not selected as suitable models for *V* due to overfitting problem (Figures 9 and 10). As for BA, the highest R^2 and the lowest total relative rank were obtained in model BA14 (Model $R^2 = 0.84$; logRMSE = 0.27, Test $R^2 = 0.77$; logRMSE = 0.33). Although models BA5 and BA13 had the same R^2 as model BA14, they were not selected as suitable models for BA due again to overfitting problems (Figures 9 and 10). For *N*, the highest R^2 and the lowest total relative rank were obtained in model N13 (Model $R^2 = 0.80$; logRMSE = 0.34, Test $R^2 = 0.70$; logRMSE = 0.37) (Figures 9 and 10). When examining the model results for h_{dom}, the highest R^2 and the lowest total relative rank were obtained in model h_{dom5} (Model $R^2 = 0.70$; logRMSE = 0.23, Test $R^2 = 0.70$; logRMSE = 0.25) (Figures 9 and 10). Finally, as for dq, the highest R^2 and the lowest total relative rank were obtained in model dq10 (Model $R^2 = 0.90$; logRMSE = 0.19, Test $R^2 = 0.80$; logRMSE = 0.26). Overall, although the R^2-values of models dq2, dq3, dq4 and dq7 were the same as model dq10 and their total relative ranks were lower, they were not selected as suitable models for dq due again to overfitting problems (Figures 9 and 10).

ANN results are given as Tables in the Supplementary material (Tables S6–S8). For volume, the model V2 performed best (Model $R^2 = 0.83$; logRMSE = 0.38, Test $R^2 = 0.77$; logRMSE = 0.47). Although the $R^2$of models V4, V6 and V7 were higher and their total relative ranks were lower, they were discarded due to overfitting. For BA, BA14 was preferred (Model $R^2 = 0.84$; logRMSE = 0.27, Test $R^2 = 0.77$; logRMSE = 0.33). BA5 and BA13 had the same R^2 but were observed to have overfitting problems. For *N*, *N*13 was preferred (Model $R^2 = 0.80$; logRMSE = 0.34, Test $R^2 = 0.70$; logRMSE = 0.37). For h_{dom}, $h_{dom}5$ was selected (Model $R^2 = 0.70$; logRMSE = 0.23, Test $R^2 = 0.70$; logRMSE = 0.25). For dq (Table S8), the highest R^2 and the lowest total relative rank were obtained in model dq10 (Model $R^2 = 0.90$; logRMSE = 0.19, Test $R^2 = 0.80$; logRMSE = 0.26). Although the coefficients of determination for models dq2, dq3, dq4 and dq7 were the same as model dq10 and their total relative ranks were lower, they were discarded as overfitted (Figures 9 and 10).

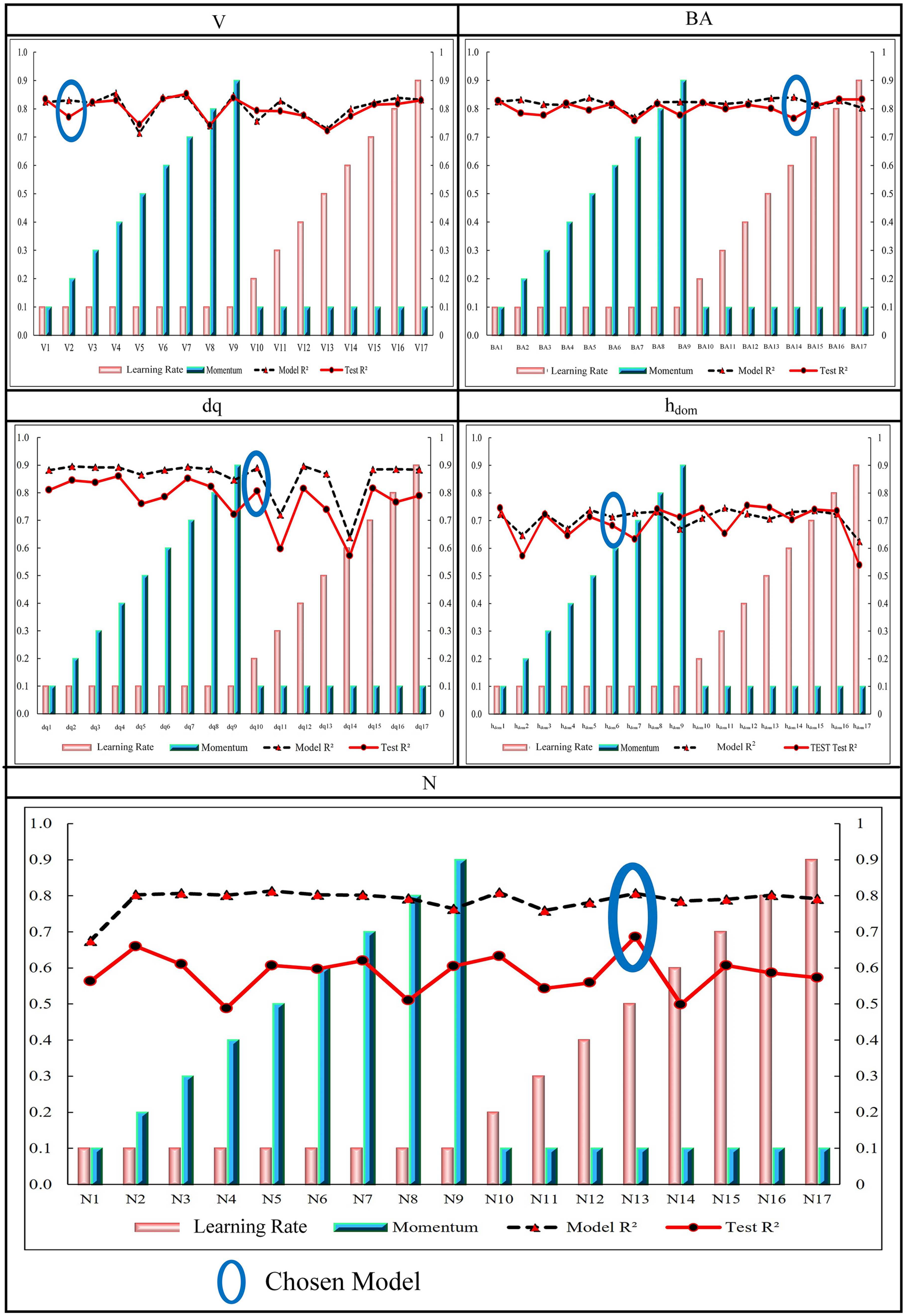

Figure 8. Coefficient of determination plots of *V*, BA, *N*, h_{dom} and dq obtained with the ANN method.

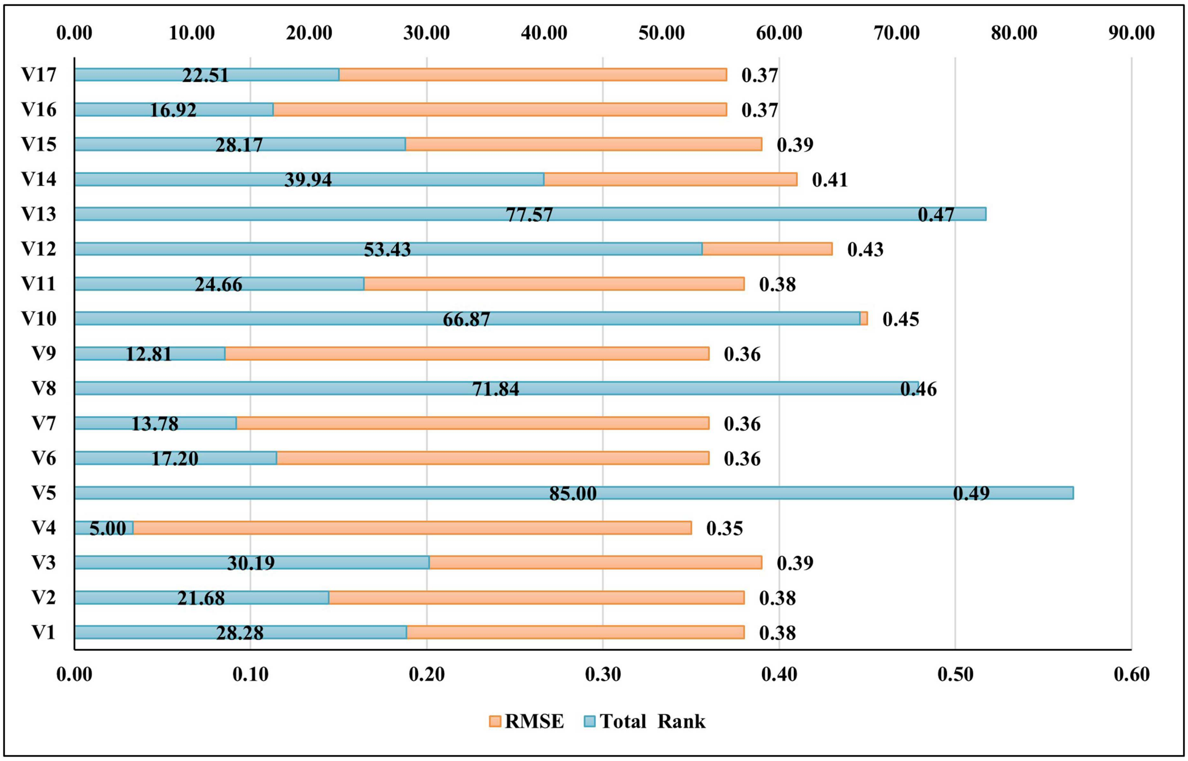

Figure 9. RMSE of models derived from remote sensing data for stand metrics with ANN and their variation with respect to total relative rank numbers (This graph for V, for the others see Supplementary material Appendix 4).

The scatter plots for the ANN applied to the test data for V, BA, N, h_{dom} and dq are also shown in Figure 10.

Bland–Altman analysis was used to MLR and ANN (Figure 11). In Figure 11, the dashed lines represent 95% confidence intervals. The center dashed line is the bias (red) and represents the average difference between the methods. The blue trend line shows the difference in the variances of the forecasts. The downward trend indicates that the first method (MLR) has a smaller variance, while the upward trend indicates that the second method (ANN) has a smaller variance. For V, a clear upward trend indicates increasing discrepancies with higher values, with ANN generally producing higher estimates, suggesting a positive bias and weak consistency. In BA, the differences are centered around zero with a nearly flat regression line, indicating overall consistency despite a few outliers, and moderate agreement. N estimates show minimal and evenly distributed differences, near-zero bias and strong alignment between methods. h_{dom}, the increasing trend in residuals at higher values suggests a systematic difference, with moderate agreement and small bias. Finally, dq displays almost no bias and very small differences, reflecting an excellent agreement between MLR and ANN.

Discussion

The present study examined relationships between forest stand variables and RS features derived from S1, S2, L8 and UAS imagery in pure Scots pine stands. The relationships were modeled using MLR and ANN.

The two-step modeling approach allows for the separation of variable selection and modeling, reducing the risk of overfitting (Dormann et al., 2013), especially with a sample size of 184 plots. Models exhibiting overfitting were consciously eliminated by testing early stopping and different learning rate and momentum combinations, with balanced results for training and test datasets being prioritized. Although methods such as random forest or LASSO can perform variable selection and nonlinear modeling simultaneously, the interpretability of variable contributions is limited, and explaining the decision process can be difficult. In contrast, MLR based variable selection is more transparent (James et al., 2013). Furthermore, training

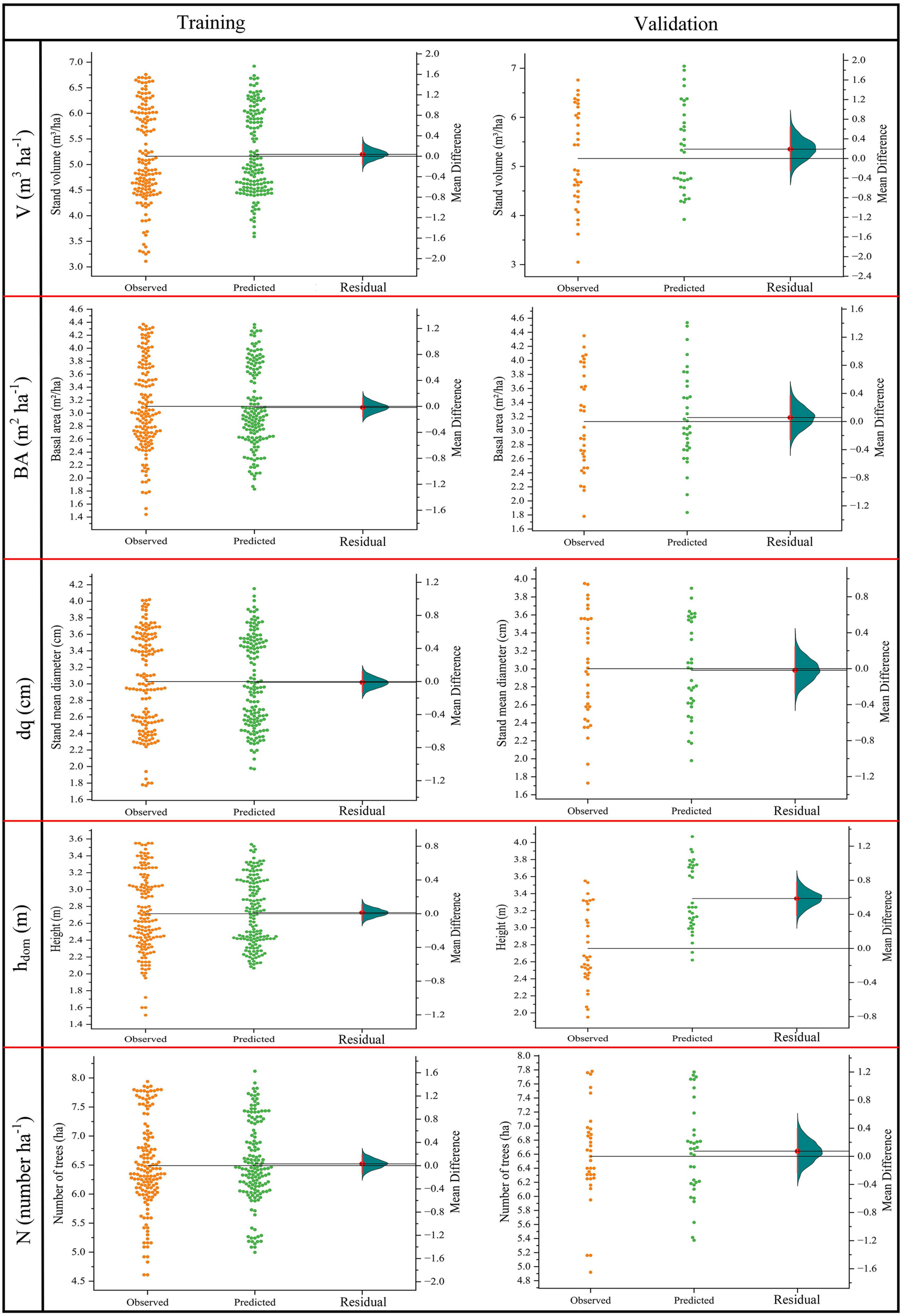

Figure 10. Observation, prediction and error scatter plot for the artificial neural network models log-transformed *V*, BA, *N*, h_{dom} and dq ANN model (for model and test).

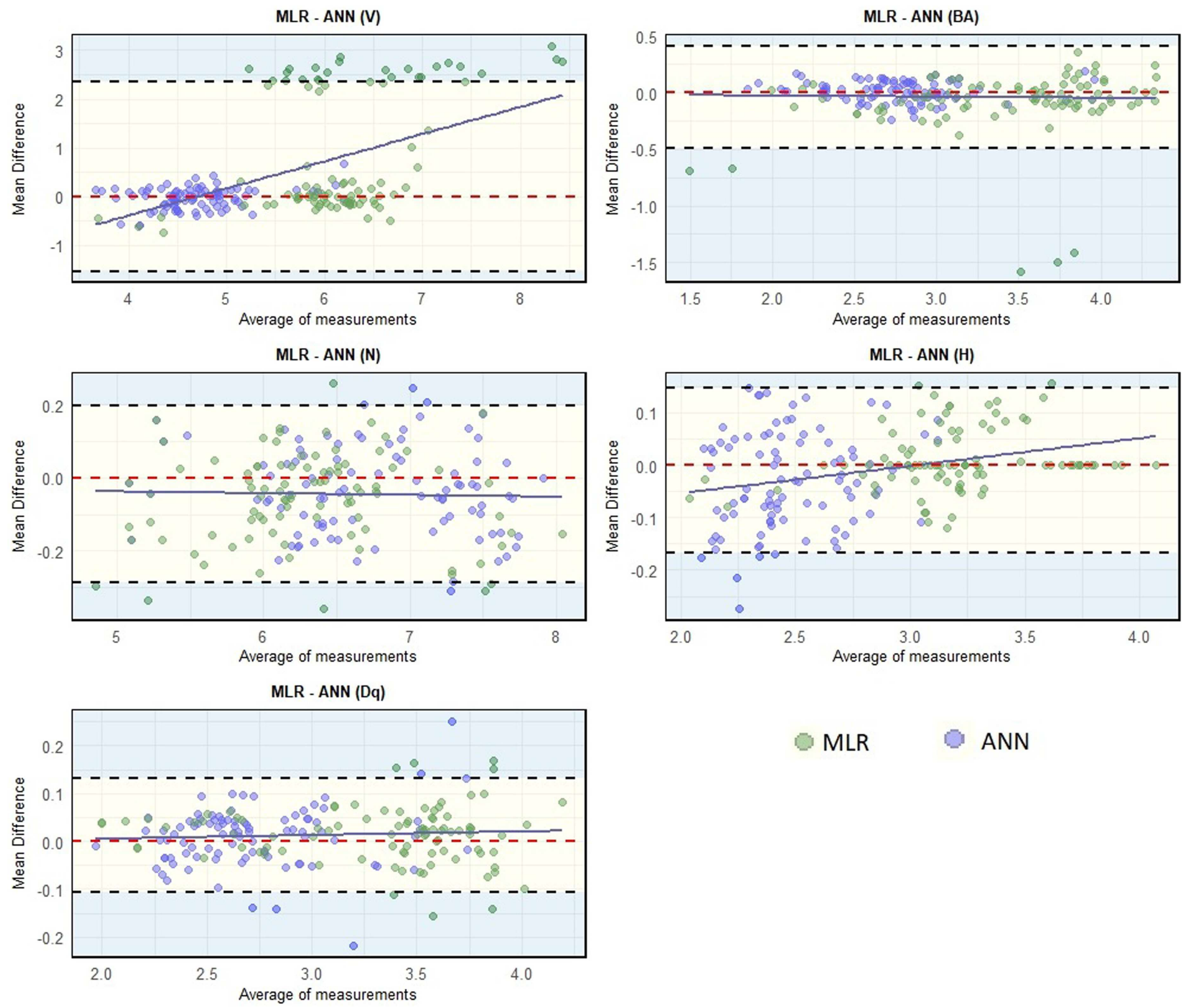

Figure 11. Bland–Altman plots of estimates of stand metrics for MLR and ANN models.

ANN models with pre-selected and statistically significant variables keeps the network structure simple and increases generalizability, thus balancing prediction accuracy with model transparency and controllability. The benefits of sequential modeling with complex ecological data have been noted before (Olden et al., 2008).

With L8 and S2 and MLR, texture features provided the highest predictive power, followed by vegetation indices and band reflectance. The lower predictive power of reflectance data may be due to image timing, solar angle, topography and forest structure, which vegetation indices are somewhat robust against which may be seen as an advantage of such indices (Ateş & Demir, 2009; Bulut, 2023b). However, models based on reflectance variables for BA and *N* provided better results than those based on vegetation indices. Similar results have been noted, e.g. by Turgut and Günlü (2022) who modeled the above-ground biomass using L8. Texture features have the advantage of being independent of color and brightness. Using texture information from several bands together can improve performance (Lee et al., 2020).

MLR performed better for *V* and h_{dom}, while ANN gave better results for BA, *N* and dq. To quantitatively contextualize the predictive performance obtained in this study, the results were compared with recent remote-sensing-based forest stand parameter studies that used S2, L8, S1, texture metrics and machine-learning or ANN based modelling approaches. Recent studies have reported a wide range of model performances depending on forest type, stand structure, target variable, plot size, sensor configuration, feature set and validation strategy. For example, Bulut et al. (2023a) reported very high predictive performance using L8 and S2 derived texture variables with machine learning methods, particularly for *N*

($R^2 = 0.98$; RMSE% = 5.97) and BA ($R^2 = 0.91$; RMSE% = 15.22). Similarly, Aksoy (2024a) reported that S2 derived datasets generally produced stronger results than L8 derived datasets, with the highest performances obtained for *V* using SVM ($R^2 = 0.78$; RMSE = 0.28 $m^3 ha^{-1}$), BA using RF ($R^2 = 0.70$; RMSE = 2.53 $m^2 ha^{-1}$) and dq using DT ($R^2 = 0.74$; RMSE = 0.02 cm). The findings of Demirel and Sakici (2025) are also particularly relevant because their study focused on pure black pine and Scots pine stands and used S1 and S2 satellite images to estimate stand diameter, number of trees, basal area, volume and stand density. Their results indicated a moderate predictive success of the derived regression models. The best models for mean diameter, basal area and number of trees were obtained using vegetation indices and texture values as independent variable groups, with reported R^2 values of 0.49, 0.34 and 0.53, respectively. These findings are consistent with the present study in two respects. First, they support the importance of S2 derived spectral and texture-based variables in estimating forest stand parameters. Second, they show that stand variables such as *N* and BA may exhibit variable and sometimes moderate prediction accuracy when modeled using optical and SAR derived predictors, depending on stand structure and data configuration. Other contemporary S2 based studies have also reported moderate but variable accuracies for forest stand parameters. Ahmadi et al. (2020), using S2 multispectral and topographic variables with several ML algorithms, reported the best BA and stem volume performance with BART (BA: $R^2 = 0.48$, RMSE = 8.12 $m^2 ha^{-1}$, stem volume: $R^2 = 0.54$, RMSE = 29.28 $m^3 ha^{-1}$), while stem density was less successfully predicted (GLM: $R^2 = 0.26$, RMSE = 53.12 n ha^{-1}). Hu et al. (2020) estimated forest stock volume using S2 imagery and reported the best test performance with RF ($R^2 = 0.58$; RMSE = 65.03 $m^3 ha^{-1}$), followed by SVR and MLR. In addition, Bolat et al. (2020) showed that L8 and S2 based regression kriging explained approximately 52% of the variance in BA and GSV, with RMSE values of 7.84 $m^2 ha^{-1}$ and 49.68 $m^3 ha^{-1}$, respectively. Texture-based and ANN-related studies further support the interpretation that spatial texture can improve forest structural parameter estimation. Günlü et al. (2021) found that WorldView-2 derived GLCM texture features produced low-to-moderate MLR performance for SV, BA, NT and AGB ($R^2 = 0.32–0.35$), whereas ANN, particularly RBF ANN, improved the prediction of SV, BA and AGB ($R^2 = 0.51–0.57$). More recently, Aksoy and Günlü (2025) reported that, in pure Scots pine stands, S2-derived 9 × 9 texture variables combined with ANN yielded the highest AGB performance ($R^2 = 0.82$, RMSE = 0.35 ton ha^{-1}). In a related AGC study, Aksoy and Günlü (2025) also reported that S2 15 × 15 texture variables with MLR produced the most successful model ($R^2 = 0.86$). When considered together, these comparisons indicate that the performance achieved in the present study falls within the range of recent S1/S2/L8, texture and ML/ANN based forest parameter estimation studies. The methodological contribution of the present study is not limited to achieving high R^2 values for selected stand parameters; rather, it lies in the systematic comparison of 31 remote-sensing-derived input datasets and in the use of a two stage MLR ANN framework, in which statistically significant predictors selected from the best-performing MLR models were transferred to the ANN stage. This approach provides a balance between predictive performance, dimensionality control and interpretability. However, direct comparison of RMSE values among studies should be interpreted cautiously because response variables, units, forest types, plot sizes, sampling designs, validation strategies and sensor combinations differ substantially among studies. Overall, studies often show that ANN and similar machine learning methods outperform MLR in predicting stand metrics. In Günlü et al. (2014), the relationships between Pan-Sharpened IKONOS band values and *V*, BA and h_{dom} were modeled with MLR, and model R^2 and RMSE performances of 0.41, 0.43 and 0.45 and 181.01 $m^3 ha^{-1}$, 14.87 $m^2 ha^{-1}$ and 4.62 m were reported, respectively. Bulut (2023b) conducted a study in pure black pine stands, in which the relationships between reflectance values obtained from L8 and S2 and *V*, BA, *N*, *h* and dq were modeled with MLR and R^2-values of 0.44, 0.41, 0.15, 0.42 and 0.23 for L8 and R^2 of 0.47, 0.45, 0.17, 0.40 and 0.25 for S2, respectively. Comparing our results with the literature, similar results have been obtained for *V* and BA, but no reasonably performing model could not be obtained for N.

The poor performance of Sentinel-1 C-band SAR data can be attributed to the short wavelength showing saturation, mostly on the canopy, in dense and closed forest stands and failing to adequately represent structural differences at the stand-level. Theoretically these limitations could be overcome by using SAR data in conjunction with optical data, though this does not always result in a meaningful and consistent performance improvement (Demirel, 2022; Nuthammachot et al., 2022), but such data fusion was outside the objectives of this study. This reflects physical constraints such as the limited penetration capacity of the C-band SAR signal and its high sensitivity to moisture and surface roughness. In addition, it is believed that the mountainous terrain of the study area may have further reduced the effectiveness of the S1 data. This is because the side-looking SAR imaging geometry is sensitive to slope- and aspect-related effects, including reflection delay, shading and local changes in the angle of incidence, and such geometric distortions can locally attenuate or enhance the backscatter signal, particularly in complex terrain (van der Woude et al., 2024). Furthermore, since C-band backscatter is primarily influenced by the upper canopy layer, its sensitivity to volumetric scattering from tree trunks and larger branches is relatively limited in dense forested areas (Rüetschi et al., 2017). Seasonal changes in canopy moisture, leaf cover status and species-specific phenological patterns have also been noted to potentially introduce temporal variability in VV and VH backscatter, thereby weakening the relationship between S1 variables and structural parameters at the tree level (Rüetschi et al., 2017; van der Woude et al., 2024). On the other hand, the longer L-band SAR signals are more sensitive to forest structure, and have been seen as more suitable, e.g. carbon and biomass applications (Wessels et al., 2023). InSAR-based products are also promising, as they can more directly represent the vertical structure of forests (He et al., 2023). Multi-source approaches can also improve performance (Xing et al., 2023). Future studies should investigate combining longer-wavelength SAR (e.g. P and L bands) with passive data, and consider UAS based hyperspectral or LiDAR sensors to enhance model accuracy, particularly for poorly predicted metrics like N. The high performance of ANN, particularly for dq, is closely related not only to the neural network structure and hyperparameter, but also to the nature of the input variables used. The dq is not a derived variable such as V or BA, but rather a fundamental stand attribute directly measured in the field, and can be more reliably predicted (Wood et al., 2012). GLCM-based texture metrics represent characteristics such as crown diameter, crown spacing and horizontal regularity within the stand, and these structural elements are strongly related to dq ecologically and geometrically. The ANN can handle complex relationships between the variables, which already have high explanatory power.

Variation in optimal GLCM window size and orientation when predicting different stand variables is closely related to forest structure and ecological characteristics. V and BA correlate with horizontal continuity of the canopy and the distribution of biomass within the stand, and larger window sizes (e.g. 9×9–15×15) effectively represent stand scale heterogeneity. For such variables, large windows can improve prediction accuracy by capturing the spatial arrangement of tree groups rather than individual trees (Fang et al., 2023a; Pu & Landry, 2012). From a mechanical perspective, wider GLCM windows combine reflection transitions between multiple canopy, canopy gap, shadow and understory components, thereby representing the continuity of canopy cover, canopy clustering and density-related heterogeneity at the stand level. These patterns are closely linked to cumulative forest characteristics such as V and BA. In contrast, smaller windows preserve contrast and edge information at the local canopy scale, which better reflects dominant tree sizes and local structural variability associated with h_{dom} and dq. This is also supported by studies showing that the optimal texture window size depends on the target forest structural variable and the spatial scale at which canopy components are represented (Ozkan & Demirel, 2018). However, satellite image texture can capture vegetation structural heterogeneity related to crown height variability and tree stem diameter (Farwell et al., 2021). In contrast, variables such as h_{dom} and dq are more sensitive to the dimensional characteristics of dominant trees within the stand, so smaller window sizes (e.g. 3×3–5×5) tend to be better suited for capturing local structural variation (Bulut et al., 2023a). N is directly related to the gap–canopy balance, horizontal distribution patterns within the stand, and spatial discontinuities. Therefore, texture metrics based on large window sizes can be useful (Wood et al., 2012). Differences in texture directions may arise in relation to crown arrangement, the dominant orientation of stand internal gaps and topographic effects. In particular, the fact that texture metrics calculated in certain directions perform better indicates that the structural patterns in the stand are not random but exhibit specific spatial orientations. The literature frequently emphasizes that tissue orientations can produce variable results depending on stand structure and that this situation can vary from ecosystem to ecosystem (Xie et al., 2008). When evaluated from a practical application perspective, testing all window size and orientation combinations for each study area can be burdensome. This burden can be significantly reduced by only testing large window sizes for V and BA, and smaller window sizes for variables related to individual tree characteristics, such as h_{dom} and dq.

In this study, the modeling of stand variables using datasets derived from UAS imagery generally yielded lower prediction accuracies compared to satellite-based data sources (L8 and S2). This can be primarily attributed to the very high spatial resolution of UAS imagery (2.5–3.5 cm), which, when processed using pixel-based and area-based approaches, introduces excessive variability and data heterogeneity. In satellite imagery, due to their coarser resolution (10–30 m), the reflectance values between forest gaps and tree crowns exhibit relatively limited variability. By contrast, UAS datasets represent the same 400–800 m^2 sample plots with approximately 45,000–50,000 pixels, which is believed to directly contribute to distorted reflectance distributions and, consequently, weakened model performance (Koger et al., 2022; Puliti et al., 2015). Therefore, the relatively low performance of UAS derived datasets should be interpreted as a consequence of applying a plot-level pixel-based/area-based workflow to centimeter-resolution imagery, rather than as a general limitation of UAS data. At this spatial scale, within-plot spectral heterogeneity may increase because crowns, shadows, gaps, understory and ground surfaces are represented separately. Future studies should consider scale aggregation, OBIA, and ITC segmentation to reduce this heterogeneity and extract crown- or tree-level structural information more effectively from UAS imagery (Gu et al., 2020; Puliti et al., 2015; Vauhkonen et al., 2012).

The higher prediction performance of S2 images compared to RGB based UAS data can be explained in terms of both spatial scale compatibility and spectral information content. S2's 10–20 m spatial resolution represents the structural characteristics of the sample plots at the stand scale in a more balanced manner and suppresses excessive reflectance variability at the tree level (Tuominen et al., 2017). In contrast, centimeter-level UAS RGB images divide the same sample plot into a very high number of pixels, increasing the effect of canopy shadows, gaps, understory and ground reflections; which can lead to heterogeneous reflectance distributions and weakened model performance in area-based/pixel-based workflows (Dainelli et al., 2021; Puliti et al., 2015). Indeed, it has been reported that maintaining the sharpest resolution in drone data does not always maximize classification/inference accuracy, intermediate resolutions can yield more balanced results (Ordóñez-Prado et al., 2024). Furthermore, it is believed that resampling UAS imagery to a coarser vegetation or canopy scale resolution could provide a direct sensitivity test for the effects of scale mismatch. However, this analysis was beyond the scope of this study, which aimed to compare UAS and satellite derived datasets using a consistent parcel-level data extraction workflow. Future studies should test different UAS collection levels to evaluate whether intermediate resolutions reduce intra-plot spectral fragmentation and improve the estimation of tree related parameters. Additionally, S2's spectral structure, which includes NIR and red-edge bands in addition to visible bands, increases sensitivity to biophysical characteristics such as chlorophyll and leaf area-canopy density, thereby providing a physical basis for estimating forest variables such as volume and basal area (Delegido et al., 2011). Furthermore, texture metrics derived from S2 have been shown to better represent forest structure and horizontal heterogeneity, thereby improving prediction power for variables such as increment and volume (Fang et al., 2023b). Several studies have demonstrated that UAS data processed using individual tree crown (ITC)-based approaches or object-based image analysis (OBIA) techniques—rather than pixel-based ABA methods result in substantially improved model accuracy (Puliti et al., 2015; Vauhkonen et al., 2012). In this context, the relatively lower accuracies observed in our study highlight the need for alternative methodological strategies, particularly ITC-based workflows, to fully exploit the potential of UAS derived data for forest parameter estimation.

Conclusions

Oriented texture features from S2 were found to be the best predictors of stand variables in pure Scots pine stands, while models based on reflectance, vegetation indices, backscatter and UAS RGB data were less effective. In general, the results obtained in this study demonstrate the potential of the approach developed for pure Scots pine stands. Future studies conducted in more heterogeneous ecosystems, such as mixed stands and broadleaf forests, will allow for a more comprehensive assessment of the model's sensitivity to species composition, horizontal heterogeneity and phenological differences. In environments with increased species diversity and structural complexity, species group or dominant species-based approaches and the use of multi-temporal optical data could improve prediction accuracy rather than a single general model. Furthermore, considering that the leafing period, phenological changes, and shading effects in broadleaf forests play a decisive role in remote-sensing-based predictions, the use of multi-temporal datasets covering different seasons is important. While texture (GLCM) based indicators have the potential to represent increasing spatial heterogeneity, it is considered that the appropriate window size and direction selection in different forest types need to be addressed more carefully. Furthermore, the extent to which the integration of SAR and optical data sources, evaluated individually in this study, can provide additional contribution compared to the use of single data sources, particularly in estimating stand parameters, should be investigated in detail in the future. In particular, when SAR data are used in conjunction with optical data, systematic comparisons should be made to determine which components of stand structure can be better represented through different wavelengths, polarizations and interferometric products. Finally, considering pure Scots pine forests in different ecological zones and under varying climate, topography and growing conditions is crucial for evaluating the generalizability of the results obtained in this study. Similar studies conducted under different ecological conditions will both clarify the limitations of the method and contribute to the development of more large-scale and reliable estimation approaches for pure Scots pine stands.

Acknowledgements

This study was produced from a doctoral thesis prepared by Hasan AKSOY and supervised by Prof. Dr. Alkan GÜNLÜ for the Institute of Natural and Applied Science, Çankırı Karatekin University, Türkiye. This study was also conducted during the author Hasan AKSOY's tenure as a visiting scientist at the Finnish Natural Resources Institute (LUKE) under the TÜBİTAK 2219 Postdoctoral Research Fellowship program (Grant no. 1059B192302166). Author Hasan AKSOY expresses his gratitude for the support provided by TÜBİTAK.

Author contributions

CRediT: **Hasan Aksoy:** Conceptualization, Data curation, Formal analysis, Funding acquisition, Methodology, Software, Validation, Visualization, Writing – original draft; **Alkan Günlü:** Investigation, Methodology, Supervision, Writing – review & editing; **Joel Kostensalo:** Funding acquisition, Investigation, Methodology, Validation, Writing – review & editing.

Disclosure statement

No potential conflict of interest was reported by the author(s).

Funding

This study was funded by the Scientific Research Project Unit of Cankırı Karatekin University (Grant No: OF211221D08). HA also received funding from Türkiye Bilimsel ve Teknolojik Araştırma Kurumu (TÜBİTAK) 2219 Postdoctoral Research Fellowship program (Grant No. 1059B192302166). JK was supported by the Research Council of Finland (Grant No: 361209).

ORCID

Joel Kostensalo 0000-0001-9883-1256

Data availability statement

The dataset used in the study is available at the following address and will be accessible to everyone upon acceptance of the article (Aksoy, 2026). https://data.mendeley.com/datasets/jcfrj2c3cv/1.

References

Ahmadi, K., Kalantar, B., Saeidi, V., Harandi, E. K., Janizadeh, S., & Ueda, N. (2020). Comparison of machine learning methods for mapping the stand characteristics of temperate forests using multi-spectral sentinel-2 data. *Remote Sensing*, *12*(18), 3019. https://doi.org/10.3390/rs12183019

Ahmed, O. S., Franklin, S. E., Wulder, M. A., & White, J. C. (2015). Characterizing stand-level forest canopy cover and height using landsat time series, samples of airborne LiDAR, and the random forest algorithm. *ISPRS Journal of Photogrammetry and Remote Sensing*, *101*, 89–101. https://doi.org/10.1016/j.isprsjprs.2014.11.007

Aksoy, H. (2022). Sinop Orman Bölge Müdürlüğü saf sarıçam meşcerelerinde farklı uzaktan algılama verileri kullanılarak bazı meşcere parametrelerinin modellenmesi (Doctoral dissertation, Doktora Tezi, Çankırı Karatekin Üniversitesi, Çankırı).

Aksoy, H. (2024a). Evaluation of forest areas and land use/cover (LULC) changes with a combination of remote sensing, intensity analysis and CA-Markov modelling. *New Zealand Journal of Forestry Science*, *54*, https://doi.org/10.33494/nzjfs542024x328x

Aksoy, H. (2024b). Estimation stand volume, basal area and quadratic mean diameter using landsat 8 OLI and Sentinel-2 satellite image with different machine learning techniques. *Transactions in GIS*, *28*(8), 2687–2704. https://doi.org/10.1111/tgis.13265

Aksoy, H. (2026). For pure Scots pine forests: Ground-based forest parameters and a dataset comprising landsat 8, Sentinel-2, Sentinel-1, and UAV-Based features. *Mendeley Data*, *V1*. https://doi.org/10.17632/jcfrj2c3cv.1

Aksoy, H., & Günlü, A. (2025). UAV and satellite-based prediction of aboveground biomass in Scots pine stands: A comparative analysis of regression and neural network approaches. *Earth Science Informatics*, *18*(1), 66. https://doi.org/10.1007/s12145-024-01657-0

Andersen, R. (2009). Nonparametric methods for modeling nonlinearity in regression analysis. *Annual Review of Sociology*, *35*, 67–85. https://doi.org/10.1146/annurev.soc.34.040507.134631

Ateş, S., & Demir, E. (2009). Uzaktan algılamada çözünürlüğe bağlı veri kazanımı potansiyeli, *TMMOB Harita ve Kadastro Mühendisleri Odası 12* (pp. 11–15). Evet, Türkiye Harita Bilimsel ve Teknik Kurultayı kurumsal bir yayıncıdır.

Bolat, F. (2021). Ankara Orman Bölge Müdürlüğü Anadolu Karaçamı meşcerelerinde artım ve büyümenin yapay sinir ağları ile modellenmesi. Doktora Tezi, Çankırı Karatekin Üniversitesi, 193 sayfa, Çankırı.

Bolat, F., Bulut, S., Günlü, A., Ercanlı, İ., & Şenyurt, M. (2020). Regression kriging to improve basal area and growing stock volume estimation based on remotely sensed data, terrain indices and forest inventory of black pine forests. *New Zealand Journal of Forestry Science*, *50*. https://doi.org/10.33494/nzjfs502020x49x

Bulut, S. (2023b). Machine learning prediction of above-ground biomass in pure calabrian pine (Pinus brutia Ten.) stands of the Mediterranean region, Türkiye. *Ecological Informatics*, *74*, 101951. https://doi.org/10.1016/j.ecoinf.2022.101951

Bulut, S., Günlü, A., & Çakır, G. (2023a). Modelling some stand parameters using landsat 8 OLI and Sentinel-2 satellite images by machine learning techniques: A case study in Türkiye. *Geocarto International*, *38*(1), 2158238. https://doi.org/10.1080/10106049.2022.2158238

Bulut, S., Günlü, A., Aksoy, H., Bolat, F., & Sönmez, M. Y. (2024). Integration of field measurements with unmanned aerial vehicle to predict forest inventory metrics at tree and stand scales in natural pure crimean pine forests. *International Journal of Remote Sensing*, *45*(12), 3846–3870. https://doi.org/10.1080/01431161.2024.2357837

Chen, W., Zheng, Q., Xiang, H., Chen, X., Sakai, T., Dainelli, R., Toscano, P., Di Gennaro, S. F., & Matese, A. (2021). Forest canopy height estimation using polarimetric interferometric synthetic aperture radar (PolInSAR) technology based on full-polarized ALOS/PALSAR.

Dainelli, R., Toscano, P., Di Gennaro, S. F., & Matese, A. (2021). Recent advances in unmanned aerial vehicle forest remote sensing—A systematic review. Part I: A general framework. *Forests*, *12*(3), 327. https://doi.org/10.3390/f12030327

David, R. M., Rosser, N. J., & Donoghue, D. N. (2022). Improving above ground biomass estimates of Southern Africa dryland forests by combining Sentinel-1 SAR and Sentinel-2 multispectral imagery. *Remote Sensing of Environment*, *282*, 113232. https://doi.org/10.1016/j.rse.2022.113232

Delegido, J., Verrelst, J., Alonso, L., & Moreno, J. (2011). Evaluation of sentinel-2 red-edge bands for empirical estimation of Green LAI and chlorophyll content. *Sensors*, *11*(7), 7063–7081. https://doi.org/10.3390/s110707063

Demirel, D. (2022). Saf karaçam ve sarıçam meşcerelerinde sentinel-1 ve sentinel-2 uydu görüntüleri yardımıyla bazı meşcere parametrelerinin tahmin edilmesi (Karadere orman işletme müdürlüğü örneği). PhD Thesis. Kastamonu Üniversitesi.

Demirel, D., & Sakici, O. E. (2025). Estimating some stand parameters using Sentinel-1 and Sentinel-2 satellite images in pure black and Scots pine stands: A case study from Türkiye. *Journal of Sustainable Forestry*, *44*(8), 729–751. https://doi.org/10.1080/10549811.2025.2529390

Dormann, C. F., Elith, J., Bacher, S., Buchmann, C., Carl, G., Carré, G., Lautenbach, S., Marquéz, J. R. G., Gruber, B., Lafourcade, B., Leitão, P. J., Münkemüller, T., McClean, C., Osborne, P. E., Reineking, B., Schröder, B., Skidmore, A. K., & Zurell, D. (2013). Collinearity: A review of methods to deal with it and a simulation study evaluating their performance. *Ecography*, *36*(1), 27–46. https://doi.org/10.1111/j.1600-0587.2012.07348.x

Dube, T., & Mutanga, O. (2015). Evaluating the utility of the medium-spatial resolution landsat 8 multispectral sensor in quantifying aboveground biomass in uMgeni catchment, South Africa. *ISPRS Journal of Photogrammetry and Remote Sensing*, *101*, 36–46. https://doi.org/10.1016/j.isprsjprs.2014.11.001

Ercanlı, İ., Kurt, A., Şenyurt, M., Günlü, A., Bolat, F., & Keleş, S. (2018). Tarsus Yöresi Anadolu Karaçamı Ağaçlarında hacim tahminlerinin yapay sinir ağları ile elde edilmesi. *Anadolu Orman Araştırmaları Dergisi*, *4*(1), 25–37.

Fang, G., He, X., Weng, Y., & Fang, L. (2023a). Texture features derived from Sentinel-2 vegetation indices for estimating and mapping forest growing stock volume. *Remote Sensing*, *15*(11), 2821. https://doi.org/10.3390/rs15112821

Fang, G., Xu, H., Yang, S. I., Lou, X., & Fang, L. (2023b). Synergistic use of Sentinel-1, Sentinel-2, and landsat 8 in predicting forest variables. *Ecological Indicators*, *151*, 110296. https://doi.org/10.1016/j.ecolind.2023.110296

Farwell, L. S., Gudex-Cross, D., Anise, I. E., Bosch, M. J., Olah, A. M., Radeloff, V. C., Pidgeon, A. M., Razenkova, E., Rogova, N., Silveira, E. M., & Smith, M. M. (2021). Satellite image texture captures vegetation heterogeneity and explains patterns of bird richness. *Remote sensing of Environment*, *253*, 112175. https://doi.org/10.1016/j.rse.2020.112175

Fassnacht, F. E., Latifi, H., Stereńczak, K., Modzelewska, A., Lefsky, M., Waser, L. T., Ghosh, A., & Straub, C. (2016). Review of studies on tree species classification from remotely sensed data. *Remote Sensing of Environment*, *186*, 64–87. https://doi.org/10.1016/j.rse.2016.08.013

Foresee, F. D., & Hagan, M. T. (1997). Gauss-Newton approximation to Bayesian learning, *Proceedings of international conference on neural networks (ICNN'97)* (Vol. *3*, pp. 1930–1935). IEEE. https://doi.org/10.1109/ICNN.1997.614194

GDF. (2022). Sinop Regional Directorate of Forestry, Forest Planning Units, Forest Management Plans. Republic of Turkey, General Directorate of Forestry, Forest Administration and Planning Department, Ankara.

Gebreslasie, M. T., Ahmed, F. B., & Van Aardt, J. A. (2010). Predicting forest structural attributes using ancillary data and ASTER satellite data. *International Journal of Applied Earth Observation and Geoinformation*, *12*, S23–S26. https://doi.org/10.1016/j.jag.2009.11.006

Gu, J., Grybas, H., & Congalton, R. G. (2020). Individual tree crown delineation from UAS imagery based on region growing and growth space considerations. *Remote Sensing*, *12*(15), 2363. https://doi.org/10.3390/rs12152363

Günlü, A., Ercanlı, İ., Şenyurt, M., & Keleş, S. (2021). Estimation of some stand parameters from textural features from WorldView-2 satellite image using the artificial neural network and multiple regression methods: A case study from Turkey. *Geocarto International*, *36*(8), 918–935. https://doi.org/10.1080/10106049.2019.1629644

Günlü, A., Ercanlı, İ., Sönmez, T., & Başkent, E. Z. (2014). Prediction of some stand parameters using pan-sharpened IKONOS satellite image. *European Journal of Remote Sensing*, *4*(1), 329–342. https://doi.org/10.5721/EuJRS20144720

Güverçin, İ., & Günlü, A. (2023). Saf Kızılçam (Pinus brutia Ten.) meşcerelerinde aktif ve pasif uydu Görüntüleri kullanılarak Topraküstü Biyokütlenin tahmin edilmesi (Anamur Orman İşletme Şefliği Örneği). *Bartın Orman Fakültesi Dergisi*, *25*(1), 177–191. https://doi.org/10.24011/barofd.1261299

Haralick, R. M., Shanmugam, K., & Dinstein, I. H. (1973). Textural features for image classification. *IEEE Transactions on Systems, Man, and Cybernetics*, SMC-3(6), 610–621. https://doi.org/10.1109/TSMC.1973.4309314

He, W., Zhu, J., Lopez-Sanchez, J. M., Gómez, C., Fu, H., & Xie, Q. (2023). Forest height inversion by combining single-baseline TanDEM-X InSAR data with external DTM data. *Remote Sensing*, *15*(23), 5517. https://doi.org/10.3390/rs15235517

Hu, Y., Xu, X., Wu, F., Sun, Z., Xia, H., Meng, Q., Xiao, X., Huang, W., Zhou, H., Gao, J., Li, W., & Peng, D. (2020). Estimating forest stock volume in Hunan Province, China, by integrating in situ plot data, Sentinel-2 images, and linear and machine learning regression models. *Remote Sensing*, *12*(1), 186. https://doi.org/10.3390/rs12010186

Hudak, A. T., Lefsky, M. A., Cohen, W. B., & Berterretche, M. (2002). Integration of lidar and Landsat ETM+ data for estimating and mapping forest canopy height. *Remote Sensing of Environment*, *82*(2-3), 397–416. https://doi.org/10.1016/S0034-4257(02)00056-1

James, G., Witten, D., Hastie, T., & Tibshirani, R. (2013). *An introduction to statistical learning* (2nd ed.). Springer. https://doi.org/10.1007/978-1-0716-1418-1

Jiang, F., Sun, H., Chen, E., Wang, T., Cao, Y., & Liu, Q. (2022). Above-ground biomass estimation for coniferous forests in Northern China using regression kriging and Landsat 9 images. *Remote Sensing*, *14*(22), 5734. https://doi.org/10.3390/rs14225734

Kalbi, S. (2011). Estimation of forest structural attributes using ASTER and SPOT-HRG data (Case study: Darabkola forest) (Doctoral dissertation, M. Sc thesis, Department of Forestry, Sari University of Agricultural Sciences & Natural Resources).

Kameyama, S., & Sugiura, K. (2020). Estimating tree height and volume using unmanned aerial vehicle photography and SfM technology, with verification of result accuracy. *Drones*, *4*(2), 19. https://doi.org/10.3390/drones4020019

Keleş, S., Günlü, A., & Ercanli, İ. (2021). Estimating aboveground stand carbon by combining Sentinel-1 and Sentinel-2 satellite data: A case study from Turkey, *Forest Resources Resilience and Conflicts* (pp. 117–126). Elsevier. https://doi.org/10.1016/B978-0-12-822931-6.00008-3

Koger, B., Deshpande, A., Kerby, J. T., Graving, J. M., Costelloe, B. R., & Couzin, I. D. (2022). Multi-animal behavioral tracking and environmental reconstruction using drones and computer vision in the wild. bioRxiv.

Krause, S., Sanders, T. G., Mund, J. P., & Greve, K. (2019). UAV-based photogrammetric tree height measurement for intensive forest monitoring. *Remote sensing*, *11*(7), 758. https://doi.org/10.3390/rs11070758

Kutser, T., Vahtmäe, E., & Praks, J. (2009). A sun glint correction method for hyperspectral imagery containing areas with non-negligible water leaving NIR signal. *Remote Sensing of Environment*, *113*(10), 2267–2274. https://doi.org/10.1016/j.rse.2009.06.016

Kwon, Y. S., Pyo, J., Kwon, Y. H., Duan, H., Cho, K. H., & Park, Y. (2020). Drone-based hyperspectral remote sensing of Cyanobacteria using vertical cumulative pigment concentration in a deep reservoir. *Remote Sensing of Environment*, *236*. 111517. https://doi.org/10.1016/j.rse.2019.111517

Latifi, H., Fassnacht, F. E., & Koch, B. (2015). Forest structure modelling with combined airborne hyperspectral and LiDAR data. *Remote Sensing of Environment*, *158*, 1–14.

Lawrence, S., Giles, C. L., & Tsoi, A. C. (1997). Lessons in neural network training: Overfitting May be harder than expected, *AAAI/IAAI* (pp. 540–545). Menlo Park, California: AAAI Press.

Lee, Y. S., Lee, S., Baek, W. K., Jung, H. S., Park, S. H., & Lee, M. J. (2020). Mapping forest vertical structure in Jeju Island from optical and radar satellite images using artificial neural network. *Remote Sensing*, *12*(5), 797. https://doi.org/10.3390/rs12050797

Lu, D. (2006). The potential and challenge of remote sensing-based biomass estimation. *International journal of remote sensing*, *27*(7), 1297–1328. https://doi.org/10.1080/01431160500486732

Mohammadi, J., Shataee, S., & Babanezhad, M. (2011). Estimation of forest stand volume, tree density and biodiversity using Landsat ETM+ data, comparison of linear and regression tree analyses. *Procedia Environmental Sciences*, *7*, 299–304. https://doi.org/10.1016/j.proenv.2011.07.052

Mutlu, M., Popescu, S. C., Stripling, C., & Spencer, T. (2008). Mapping surface fuel models using lidar and multispectral data fusion for fire behavior. *Remote Sensing of Environment*, *112*(1), 274–285. https://doi.org/10.1016/j.rse.2007.05.005

Nuthammachot, N., Askar, A., Stratoulias, D., & Wicaksono, P. (2022). Combined use of Sentinel-1 and Sentinel-2 data for improving above-ground biomass estimation. *Geocarto International*, *37*(2), 366–376. https://doi.org/10.1080/10106049.2020.1726507

Okut, H. (2016). Bayesian regularized neural networks for small n big p data. *Artificial neural networks-models and applications*, *28*, https://doi.org/10.5772/63256

Olden, J. D., Lawler, J. J., & Poff, N. L. (2008). Machine learning methods without tears: A primer for ecologists. *The Quarterly review of biology*, *83*(2), 171–193. https://doi.org/10.1086/587826

Ordóñez-Prado, C., Valdez-Lazalde, J. R., Flores-Magdaleno, H., Ángeles-Pérez, G., Santos-Posadas, H. M., & Buendía-Rodríguez, E. (2024). Operational implications of spatial resolution of drone imagery in vegetation mapping for forestmanagement. *Revista Chapingo serie ciencias forestales y del ambiente*, *30*(2), 1–18. https://doi.org/10.5154/r.rchscfa.2023.06.040

Ozkan, U. Y., & Demirel, T. (2018). Estimation of forest stand parameters by using the spectral and textural features derived from digital aerial images. *Applied Ecology & Environmental Research*, *16*(3), 3043–3060. https://doi.org/10.15666/aeer/1603_30433060

Ozkan, U. Y., Ertekin, C., & Akyuz, A. (2012). Estimation of forest stand parameters using artificial neural networks and multiple linear regression models. *Environmental Monitoring and Assessment*, *184*(5), 2803–2814.

Phiri, D., & Morgenroth, J. (2017). Developments in Landsat land cover classification methods: A review. *Remote Sensing*, *9*(9), 967. https://doi.org/10.3390/rs9090967

Poudel, K. P., & Cao, Q. V. (2013). Evaluation of methods to predict Weibull parameters for characterizing diameter distributions. *Forest Science*, *59*(2), 243–252. https://doi.org/10.5849/forsci.12-001

Pu, R., & Landry, S. (2012). A comparative analysis of high spatial resolution IKONOS and WorldView-2 imagery for mapping urban tree species. *Remote Sensing of Environment*, *124*, 516–533. https://doi.org/10.1016/j.rse.2012.06.011

Puliti, S., Ørka, H. O., Gobakken, T., & Næsset, E. (2015). Inventory of small forest areas using an unmanned aerial system. *Remote Sensing*, *7*(8), 9632–9654. https://doi.org/10.3390/rs70809632

Qiu, Y., Huang, J., Luo, J., Xiao, Q., Shen, M., Xiao, P., Duan, H., Peng, Z., & Jiao, Y. (2025). Monitoring, simulation and early warning of cyanobacterial harmful algal blooms: An upgraded framework for eutrophic lakes. *Environmental Research*, *264*, 120296. https://doi.org/10.1016/j.envres.2024.120296

Rüetschi, M., Schaepman, M. E., & Small, D. (2017). Using multitemporal sentinel-1 c-band backscatter to monitor phenology and classify deciduous and coniferous forests in Northern Switzerland. *Remote Sensing*, *10*(1), 55. https://doi.org/10.3390/rs10010055

SAKICI, O. E., & GÜNLÜ, A. (2018). ARTIFICIAL INTELLIGENCE APPLICATIONS FOR PREDICTING SOME STAND ATTRIBUTES USING LANDSAT 8 OLI SATELLITE DATA: A CASE STUDY FROM TURKEY. Applied Ecology and Environmental Research, 5269–5285. http://dx.doi.org/10.15666/aeer/1604_52695285

Shi, K., Zhang, Y., Qin, B., & Zhou, B. (2019). Remote sensing of cyanobacterial blooms in inland waters: Present knowledge and future challenges. *Science Bulletin*, *64*(20), 1540–1556. https://doi.org/10.1016/j.scib.2019.07.002

Sinha, S., Jeganathan, C., Sharma, L. K., & Nathawat, M. S. (2015). A review of radar remote sensing for biomass estimation. *International Journal of Environmental Science and Technology*, *12*, 1779–1792. https://doi.org/10.1007/s13762-015-0750-0

Skudnik, M., & Jevšenak, J. (2022). Artificial neural networks as an alternative method to nonlinear mixed-effects models for tree height predictions. *Forest Ecology and Management*, *507*, 120017. https://doi.org/10.1016/j.foreco.2022.120017

Thanh Noi, P., & Kappas, M. (2017). Comparison of random forest, k-nearest neighbor, and support vector machine classifiers for land cover classification using Sentinel-2 imagery. *Sensors*, *18*(1), 18. https://doi.org/10.3390/s18010018

Tuominen, S., & Haakana, M. (2005). Landsat TM imagery and high altitude aerial photographs in estimation of forest characteristics.
Tuominen, S., Pitkänen, T., Balazs, A., & Kangas, A. (2017). Improving Finnish multi-source national forest inventory by 3D aerial imaging. *Silva Fennica*, *51*(4), 7743. https://doi.org/10.14214/sf.7743
Turgut, R., & Günlü, A. (2022). Estimating aboveground biomass using Landsat 8 OLI satellite image in pure Crimean pine (Pinus nigra JF Arnold subsp. pallasiana (Lamb.) Holmboe) stands: A case from Turkey. *Geocarto International*, *37*(3), 720–734. https://doi.org/10.1080/10106049.2020.1737971
van der Woude, S., Reiche, J., Sterck, F., Nabuurs, G. J., Vos, M., & Herold, M. (2024). Sensitivity of sentinel-1 backscatter to management-related disturbances in temperate forests. *Remote Sensing*, *16*(9), 1553. https://doi.org/10.3390/rs16091553
Vauhkonen, J., Ene, L., Gupta, S., Heinzel, J., Holmgren, J., Pitkänen, J., Maltamo, M., Pitkanen, J., Solberg, S., Wang, Y., Weinacker, H., Hauglin, K. M., Lien, V., Packalen, P., Gobakken, T., Koch, B., Naesset, E., & Tokola, T. (2012). Comparative testing of single-tree detection algorithms under different types of forest. *Forestry*, *85*(1), 27–40. https://doi.org/10.1093/forestry/cpr051
Were, K., Bui, D. T., Dick, [., & Singh, B. R. (2015). A comparative assessment of support vector regression, artificial neural networks, and random forests for predicting and mapping soil organic carbon stocks across an afromontane landscape. *Ecological Indicators*, *52*, 394–403. https://doi.org/10.1016/j.ecolind.2014.12.028
Wessels, K., Li, X., Bouvet, A., Mathieu, R., Main, R., Naidoo, L., Asner, G. P., & Erasmus, B. (2023). Quantifying the sensitivity of L-Band Sar to a decade of vegetation structure changes in savannas. *Remote Sensing of Environment*, *284*, 113369. https://doi.org/10.1016/j.rse.2022.113369
White, J. C., Coops, N. C., Wulder, M. A., Vastaranta, M., Hilker, T., & Tompalski, P. (2016). Remote sensing technologies for enhancing forest inventories: A review. *Canadian Journal of Remote Sensing*, *42*(5), 619–641. https://doi.org/10.1080/07038992.2016.1207484
Wood, E. M., Pidgeon, A. M., Radeloff, V. C., & Keuler, N. S. (2012). Image texture as a remotely sensed measure of vegetation structure. *Remote Sensing of Environment*, *121*, 516–526. https://doi.org/10.1016/j.rse.2012.01.003
Wu, C., Shen, H., Shen, A., Deng, J., Gan, M., Zhu, J., Wang, K., & Xu, H. (2016). Comparison of machine-learning methods for above-ground biomass estimation based on Landsat imagery. *Journal of Applied Remote Sensing*, *10*(3), 035010–035010. https://doi.org/10.1117/1.JRS.10.035010
Xie, Y., Sha, Z., & Yu, M. (2008). Remote sensing imagery in vegetation mapping: A review. *Journal of Plant Ecology*, *1*(1), 9–23. https://doi.org/10.1093/jpe/rtm005
Xing, C., Wang, H., Zhang, Z., Yin, J., & Yang, J. (2023). A review of forest height inversion by PolInSAR: Theory, advances, and perspectives. *Remote Sensing*, *15*(15), 3781. https://doi.org/10.3390/rs15153781
Yavuz, H., Mısır, N., Tüfekçioğlu, A., Altun, L., Mısır, M., Ercanlı, İ., Sakıcı, O. E., Kahriman, A., Karahalil, U., Yılmaz, M., Sarıyıldız, T., Küçük, M., Meydan, G., Bayburtlu, Ş., Bilgili, F., Aydın, A. C., Kara, Ö, Bolat, İ., & ve Usta, A. (2010). Karadeniz Bölgesi saf ve karışık Sarıçam (*Pinus slyvestris* L.) meşcereleri için mekanistik büyüme modellerinin geliştirilmesi, biyokütle ve karbon depolama miktarlarının belirlenmesi. (TÜBİTAK-TOVAG Projesi, Proje No: 106O274), Karadeniz Teknik Üniversitesi Orman Fakültesi, Trabzon.
Zahriban Heasari, M., Fallah, A., Shataee, S., Kalbi, S., & Persson, H. (2019). ESTIMATING THE FOREST STAND VOLUME AND BASAL AREA USING PLEIADES SPECTRAL AND AUXILIARY DATA. Int.Arch. Photogramm. Remote Sens. Spatial Inf. Sci., XLII-4/W18, 1131–1136. https://doi.org/10.5194/isprs-archives-XLII-4-W18-1131-2019
Zhang, L., Wang, Y., Song, X. P., & Townshend, J. R. (2019). Estimating forest stand attributes from remote sensing data using neural networks and regression trees. *International Journal of Applied Earth Observation and Geoinformation*, *76*, 58–70.
Zhao, Q., Yu, S., Zhao, F., Tian, L., & Zhao, Z. (2019). Comparison of machine learning algorithms for forest parameter estimations and application for forest quality assessments. *Forest Ecology and Management*, *434*, 224–234. https://doi.org/10.1016/j.foreco.2018.12.019